UNIVERSITY OF CALIFORNIA,
IRVINE

Real-time, quantitative assessment of tissue oxygen metabolism and hemodynamics using coherent light

DISSERTATION

submitted in partial satisfaction of the requirements
for the degree of

DOCTOR OF PHILOSOPHY

in Biomedical Engineering

by

Michael Ghijsen

Dissertation Committee:
Professor Bruce J. Tromberg, Chair
Professor Anthony J. Durkin
Professor Bernard Choi

2018

DEDICATION

To

my parents, Walter and Susan Ghijsen

TABLE OF CONTENTS

LIST OF FIGURES

LIST OF TABLES

ACKNOWLEDGMENTS

I am deeply grateful to my mentor and committee chair Professor Bruce J. Tromberg for his kindness, vision, and expertise. Bruce went above and beyond in providing not only resources for this work but also opportunities for my professional development and travel. More importantly, his dedication to mentorship and attention to detail pushed me to produce my best possible work. In addition, he fostered a work environment that balanced freedom and independence with productivity and impact.

My sincere thanks also go to the members of my dissertation committee and our collaborators. Thank you to Professor Anthony Durkin for his mentorship and relentless practicality; he is quite possibly the most logical and inquisitive people I have ever met. Thank you to my undergraduate research advisor Professor Gultekin Gulsen whose initial inspiration helped me decide to become a scientist. I thank Professor Sylvain Gioux for his help and expertise in optics and signal processing. Thank you also to Professor Vasan Venugopalan for his commitment to education and for fostering the BEST IGERT program which provided financial support for half of my graduate education. I also wish to thank Professor Bernard Choi for his expertise and advice regarding Laser Speckle Imaging.

I would like to express gratitude to the postdoctoral fellows and graduate students without whom this work would not have been possible. I thank Dr. Adrien Ponticorvo and Dr. Rolf Sager for their optical engineering expertise, which directly helped me design and troubleshoot the major instrument builds in this work. I thank Dr. Robert Wilson, Mohammad Torabzadeh, Robert Warren, Rebecca Rowland, and Kyle Nadeau. I would also like to thank the members of Laser Associated Sciences, Tyler Rice, Sean White, and Bruce Yang, for their contribution to this work.

A special thanks to Dr. Gordon Kennedy for his commitment to teaching and his endless patience. He consistently puts the needs of others above his own.

I thank the Optics Society of America (OSA) for permission to include Chapters 2 and 4 which were originally published in Biomedical Optics Express. I also thank the International Society for Optics and Photonics (SPIE) for permission to include Chapter 3 which was original published in the Journal of Biomedical Optics.

I acknowledge funding provided by the NIH NIBIB Biomedical Technology Research Center LAMMP P41EB015890, the Military Medical Photonics Program, AFOSR Grant No. FA9550-08-1-0384, the Arnold and Mabel Beckman Foundation, the NIH NHLBI Ruth L. Kirschstein National Research Service award 5-F30-HL132481-02, the BEST IGERT program funded by the National Science Foundation DGE-1144901, and the Medical Scientist Training Program funded by the National Institutes of Health T32-GM08620.

CURRICULUM VITAE

Michael Thomas Ghijsen

2009 B.S. in Physics, University of California, Irvine

2016 M.S. in Biomedical Engineering, University of California, Irvine

2018 Ph.D. in Bioemedical Engineering, University of California, Irvine

FIELD OF STUDY

Biophotonics

PUBLICATIONS

1. **M. Ghijsen**, G.R. Lentsch, S. Gioux, M. Brenner, A.J. Durkin, B. Choi, B.J. Tromberg, "Quantitative real-time optical imaging of the tissue metabolic rate of oxygen consumption", Journal of Biomedical Optics 23.3 (2018): 036013.

2. **M. Ghijsen**, B. Choi, A.J. Durkin, S. Gioux, B.J. Tromberg, "Real-time simultaneous single snapshot of optical properties and blood flow using coherent spatial frequency domain imaging (cSFDI)", Biomedical Optics Express 7.3 (2016): 870-882.

3. **M. Ghijsen**, Y. Lin, M. Hsing, O. Nalcioglu, G. Gulsen, "Optimal analysis method for dynamic contrast-enhanced diffuse optical tomography. Journal of Biomedical Imaging (2011): 7.

4. Y. Lin, **M. Ghijsen**, O. Nalcioglu, G. Gulsen, "In vivo quantitative frequency domain fluorescence tomography", Journal of biomedical optics 17.12 (2012): 126021-126021.

5. Y.Lin, L. Bolisay, **M. Ghijsen**, T.C. Kwong, G. Gulsen, "Temperature-modulated fluorescence tomography in a turbid media", Applied physics letters 100.7 (2012): 073702.

6. Y. Lin, **M. Ghijsen**, H. Gau, N. Liu, O. Nalcioglu, G. Gulsen, "A phto-multiplier tube-based hybrid MRI and frequency domain fluorescence tomography system for small animal imaging", Physics in medicine and biology 56.15 (2011): 4731.

PATENTS

1. **M. Ghijsen**, T.B. Rice, S. White, B.J. Tromberg, B. Yang "Non-invasive hemodynamic assessment via interrogation of biological tissue using a coherent light source." UCI009.048A

PRESENTATIONS

1. **M. Ghijsen**, A.J. Durkin, B.J. Tromberg, "Real-time quantitative assessment of tissue oxygen metabolism using Coherent Spatial Frequency Domain Imaging (cSFDI)", Annual MSTP Student Symposium, Irvine, CA, February 2017

2. **M. Ghijsen**, A.J. Durkin, B.J. Tromberg, "Real-time quantitative assessment of tissue oxygen metabolism using Coherent Spatial Frequency Domain Imaging (cSFDI)" Biomedical Engineering Student Symposium, Irvine, CA, March 2017.

3. **M. Ghijsen**, A.J. Durkin, B.J. Tromberg, "Algorithmic processing of intrinsic signals in affixed transmission speckle analysis (ATSA)", SPIE Photonics West, BiOS, San Francisco, CA, February 2017.

4. **M. Ghijsen**, A.J. Durkin, B.J. Tromberg , "Intrinsic signals in space and time: real-time quantitative mapping of tissue optical properties and flow." MSTP Annual Scientific Retreat, Lake Arrowhead, CA, October 2015

5. **M. Ghijsen**, A.J. Durkin, B.J. Tromberg, "Intrinsic Signals in Space and Time", MD PhD National Student Conference, Keystone, Co, July 2015.

6. **M. Ghijsen**, A.J. Durkin, B.J. Tromberg, "Measuring tissue oxygen consumption with coherent single snapshot optical properties (cSSOP)", Annual MSTP Student Symposium, Irvine, CA, March 2015

7. **M. Ghijsen**, A.J. Durkin, S. Gioux, B.J. Tromberg, "Imaging metabolic oxygen consumption using coherent single snapshot optical properties (cSSOP)", SPIE Photonics West, BiOS, San Francisco, CA, February 2015.

ABSTRACT OF THE DISSERTATION

Real-time, quantitative assessment of tissue oxygen metabolism
and hemodynamics using coherent light

By

Michael Thomas Ghijsen

Doctor of Philosophy in Biomedical Engineering

University of California, Irvine, 2018

Professor Bruce J. Tromberg, Chair

Tissue metabolism and hemodynamics are known to be abnormal in several pathologies. Peripheral arterial disease is one such example where tissue metabolism is reduced as an adaptive mechanism to hypoxia. In this same disease, pulsatile hemodynamic signatures are deteriorated by progressive arterial obstruction. Interrogating tissue with coherent light sources offers a simple and effective means for noninvasive cardiovascular assessment by directly measuring tissue oxygen metabolism and pulsatile hemodynamics.

In this work we develop a wide-field, noncontact imaging technique that utilizes coherent light and pixel-based detectors to map metabolism and blood flow at high speeds. First, we expand upon previous work on Coherent Spatial Frequency Domain Imaging (cSFDI) by mitigating bottlenecks in data acquisition. Adapting advanced image demodulation techniques along with simplified projection optics, we are able to recover the tissue absorption and reduced-scattering coefficients (μ_a and μ_s', respectively), in addition to speckle contrast from a single snapshot. Next, we extend this technique to two wavelengths allowing for the recovery blood flow, oxyhemoglobin and deoxyhemoglobin at

16 frames per second. We then implement a framework for extracting the tissue metabolic rate of oxygen consumption ($tMRO_2$). We validate $tMRO_2$ measurements using yeast-hemoglobin phantoms in which oxygen is progressively extracted from bovine hemoglobin with baker's yeast. As a proof of concept, we perform a series of *in vivo* arterial occlusion protocols and demonstrate sensitivity to metabolic changes caused by transient tissue ischemia. Finally, we sequence a rabbit model of cyanide poisoning showing that cSFDI is capable of recovering metabolic dynamics consistent with mitochondrial uncoupling.

At the same time, we investigate pulsatile signals due to the cardiac cycle using a novel device that measures coherent speckle patterns in *transmission* geometry; this technique is called Affixed Transmission Speckle Analysis (ATSA). From a single coherent light source, we obtain two signals, one related to blood flow and one related to vascular compliance. We demonstrate sensitivity to arterial stiffness and vascular tone using novel processing methods aimed at characterizing timing offsets between the signals along with embedded harmonic content. Our results suggest that parameters extracted using our processing methods are sensitive to both arterial stiffness and vascular tone. Overall, this work demonstrates that coherent light-based techniques constitute a promising low-cost strategy for noninvasive cardiovascular assessment.

CHAPTER 1: INTRODUCTION

Many diseases are caused by aberrations in tissue metabolism due to adaptations to local cellular conditions [1-3]. For example, abnormal metabolism present in cancer fuels rapid cellular growth while maintaining relative insensitivity to oxygen supply [4]. In Peripheral Arterial Disease, a silently progressive condition caused by long-term atherosclerosis, tissue is subject to decreased perfusion in peripheral circulation [5]. In this situation, oxygen consumption is down-regulated in response to chronically low oxygen tension. Coronary artery disease, chronic wounds, diabetes, and neurodegenerative diseases all contain similar features [5-8]. In each condition, quantitative dynamic imaging of the tissue metabolic rate of oxygen consumption ($tMRO_2$) could provide an approach to screening, diagnosis and therapeutic monitoring.

Positron emission tomography (PET) is an example of an existing method that characterizes $tMRO_2$ [9]. In this technique, fluorodeoxyglucose is administered intravenously and accumulates in regions of high tissue metabolism, emitting two gamma rays in opposite directions when the fluoride isotope decays. The PET system detects these gamma rays, triangulating on their position to localize metabolic activity. The main shortcoming is that PET employs exogenous radioactive contrast agents, limiting its utility for more routine applications. Functional magnetic resonance imaging (fMRI) also measures metabolic activity via the blood oxygen level dependent (BOLD) signal [10]. fMRI characterizes $tMRO_2$ by taking advantage of the different spin magnetic properties of oxy- and deoxyhemoglobin. Although fMRI is noninvasive and requires no exogenous contrast, the technique is extremely time-consuming and expensive.

Optical imaging and spectroscopic methods constitute a unique strategy for inexpensive noninvasive metabolic measurements. Diffuse Optical Spectroscopy (DOS) is one example of an optical method that measures hemodynamic and biochemical composition in centimeter-thick tissues [11-13], while Diffuse Correlation Spectroscopy (DCS) is a complimentary technique that measures relative blood flow [14, 15]. Together, DOS and DCS can characterize tissue metabolic activity [16]. However, DOS-DCS is only capable of point-by-point measurements using contact probes, impacting the utility in compromised tissues such as an open wound and in heterogeneous regions where single point measurements are not sufficient.

Spatial Frequency Domain Imaging (SFDI) is a noncontact imaging technique capable of mapping tissue optical properties that addresses these shortcomings [17, 18]. Like DOS, SFDI is incapable of directly measuring perfusion such that it cannot independently determine tissue metabolism in the presence of blood flow. Laser Speckle Imaging (LSI) is a similar wide-field technique utilizing coherent light to generate maps of relative perfusion[19, 20]. Together, SFDI and LSI can image $tMRO_2$ by synthesizing chromophore concentrations and relative blood flow.

Coherent Spatial Frequency Domain Imaging (cSFDI) combines LSI and SFDI using a spatially modulated coherent light to recover the absorption coefficient (μ_a) , the reduced-scattering coefficient (μ_s'), and speckle contrast in superficial tissues up to approximately 5 mm in depth [21-25]. cSFDI quantitatively maps concentrations of oxy- and deoxyhemoglobin ([HbO_2] and [HHb], respectively) by measuring μ_a at multiple discrete wavelengths. Simultaneously, speckle contrast obtained with the same raw data is converted to a measurement of relative blood flow known as Speckle Flow Index (SFI)[22,

26-30]. This technique can extract $tMRO_2$ from this information by invoking Fick's principle to synthesize chromophore concentrations and blood flow [31, 32]. However, the amount of raw data needed to reconstruct a single $tMRO_2$ time-point represents a practical limitation of this technology, restricting the acquisition speed and resulting loss of dynamic metabolic information.

Signal processing techniques have recently been applied to spatial frequency domain method to demodulate data with fewer raw images [33, 34]. One method is capable of extracting tissue optical properties from a single snapshot of raw data, reducing the number of raw images by a factor of 6 [33]. This techniques functions using Discrete Fourier Transforms with frequency domain filters to demodulate two spatial frequencies from a single image. Referred to as Single Snapshot Optical Properties (SSOP) imaging, this method reduces the number of frames by a factor of 6 allowing for real-time data acquisition. Additionally, SSOP allows for the use of a static objects as a spatial light modulator since only a single pattern is needed to reconstruct images. This contrasts with conventional demodulation approaches requiring multiple patterns and demanding the use of a computer controlled spatial light modulator such as a digital micromirror device or liquid crystal on silicon chip. In summary, the ability to extract all necessary information from a single image produces real-time property acquisition and simplified cost-effective instrumentation.

In this work we present the development and validation of high-speed coherent spatial frequency domain imaging for the high-speed imaging of $tMRO_2$. In Chapter 2 we lay out the development of single snapshot coherent spatial frequency domain imaging. We begin by assembling a single-wavelength coherent spatial frequency domain imaging apparatus

that uses a single fixed pattern and a high speed sCMOS camera. We then apply previously-developed advanced demodulation techniques and validate the imaging system on standardized phantoms with known optical properties. In Chapter 3 we present the development of methods for intrinsic signal processing derived from a finger-clip wearable device referred to as Affixed Transmission Speckle Analysis (ATSA). Several human subjects being measured with the ATSA device undergo physiologic challenges. Sensitivity to physiologic adaptation is demonstrated using our processing methods. Additionally, we demonstrate strong correlations between arterial stiffness and extracted physiologic parameters. In Chapter 4 we outline the development of the dual-wavelength high-speed single-snapshot cSFDI with the goal of $tMRO_2$ imaging in real-time. Using two wavelengths, we show the decoupling of oxy- and deoxyhemoglobin in addition to the measurement of relative blood flow; these metrics are then synthesized into oxygen metabolic measurements. Finally, this system is tested on an animal model of cyanide poisoning and *in vivo* human experiments.

CHAPTER 2: SINGLE SNAPSHOT COHERENT SPATIAL FREQUENCY DOMAIN IMAGING

2.1 Attaining high frame rates

In this chapter we describe the method for increasing the frame rate of cSFDI. This is done by mitigating bottle necks in data acquisition. To give the proper context, cSFDI utilizes the Spatial Frequency Domain (SFD) methods to decouple μ_a and μ_s'. These methods, which have been previously described in detail [17, 18], employ structured illumination to interrogate the light-tissue interaction. Fundamentally, SFD methods are aimed at recovering the diffuse modulation transfer function. This is done by projecting multiple sinusoidal patterns over a range of spatial frequencies onto the sample of interest, and then imaging the resulting distortion (caused by the sample) of the sinusoidal pattern. Computational models of photon transport are then applied to these measurements in order to calculate μ_a and μ_s'. By acquiring μ_a at multiple optical wavelengths, the Beer-Lambert law can be invoked to recover the concentration of tissue chromophores such as oxyhemoglobin, deoxyhemoglobin, water and lipid [25, 35]. In addition, μ_s' can reveal information pertaining to tissue structure and orientation [34, 36].

The bottleneck in data acquisition comes from the amount raw data needed to recover optical properties (μ_a and μ_s') at a single optical wavelength. Using conventional methods, optical properties require demodulating 2 spatial frequencies each with 3 spatial phases [17, 18, 34] for a total of 6 raw images. Recently, signal processing techniques have been applied to SFD methods to demodulate data with fewer raw images [33, 34]. One such method, introduced by Vervandier et al. is capable of extracting tissue optical properties from a single frame of raw data, reducing the number of raw images by a factor of 6 [33,

37]. This technique applies spatial Discrete Fourier Transforms and frequency domain processing to demodulate two frequencies from a single frame of raw data. In comparison with conventional demodulation method, this approach – referred to as Single Snapshot of Optical Properties (SSOP) – reduces the number of frames by a factor of 6, allowing for real-time mapping of optical properties. Perhaps more importantly, SSOP allows for the use of static objects as spatial light modulators since only a single pattern is needed to recover optical properties. This is in contrast to conventional demodulation approaches which require multiple patterns demanding the use of computer controlled spatial light modulators such as a Digital Micromirror Device (DMD) or Liquid Crystal on Silicon (LCOS) chips. In short, the ability to extract all the necessary information from a single image allows for real-time property acquisition and simplified cost-effective instrumentation.

In this chapter, we present our work on the application of SSOP demodulation to cSFDI to extract optical properties *and* speckle contrast from a single snapshot. We present the algorithmic implementation of SSOP demonstrating the steps required to extract μ_a, μ_s', and SFI from a single image of spatially modulated coherent light. In addition, we introduce a simple cSFDI instrument-build that requires only one sinusoidal-patterned slide to achieve spatial light modulation. Next, in two *in vitro* experiments we present data validating single snapshot cSFDI in comparison with conventional techniques. In the first set of experiments we use homogeneous phantoms to demonstrate our ability to accurately recover bulk optical properties. In the second validation experiment we use a flow-phantom to compare single snapshot cSFDI with conventional LSI in terms of sensitivity to changes in flow speed. Finally, we report on *in vivo* experiments on a human forearm undergoing post-occlusive reactive hyperemia via a cuff-occlusion-release protocol. The *in vivo* data

demonstrate sensitivity to intrinsic physiological signals such as the accumulation of deoxyhemoglobin in occluded tissue and heartbeat fluctuations observed from SFI values. Although optical property correction can be performed on flow measurements, this computational step is left to future studies.

2.2 Methods

2.2.1 Single snapshot cSFDI instrumental setup

A 120 mW 660 nm laser diode (HL6545MG Opnext Inc.) was powered and stabilized using a combined laser diode and temperature controller (Newport Corporation). Coherent light from the laser diode was spatially homogenized using a ground glass diffuser and then condensed onto a sinusoidal-patterned slide (Applied Image Inc.). The pattern was imaged onto the sample using an objective lens in off-axis configuration. The sinusoidal projection pattern had a fixed spatial frequency of 0.185 mm^{-1}. Data was recorded using a high-speed sCMOS camera (Hamamatsu Photonics, Orca Flash 4.0) with a cross polarizer placed in front of a 16 mm fixed focal length lens (Edmund Optics). For all experiments mentioned below, the lens aperture was f/5.6 and the integration time was 20 ms, allowing for a data acquisition rate of 50 frames per second. The aperture and integration time were set to manage the trade-off in accuracy between speckle contrast and optical properties.

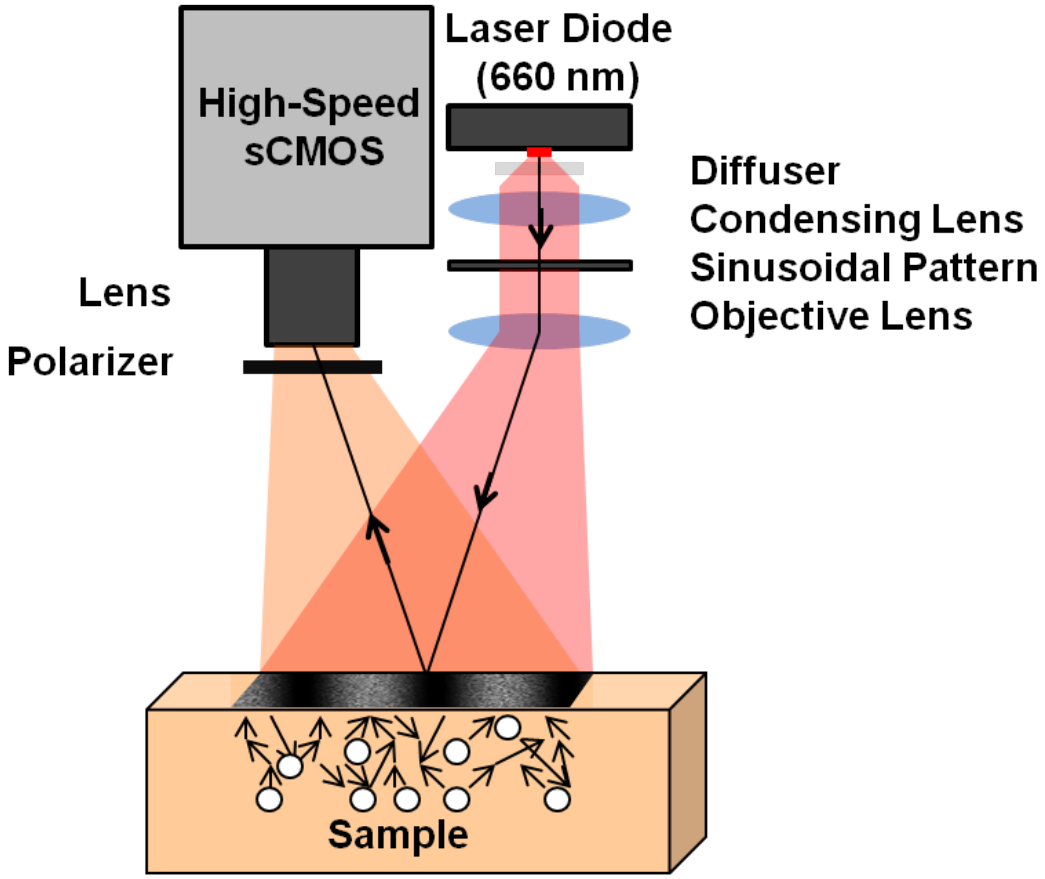

Figure 2.1 Experimental setup. Light from a coherent source is spatially modulated and projected onto a diffuse medium. Remitted light from the sample is collected using a high-speed sCMOS camera.

2.2.2 Three-phase demodulation from conventional SFDI

Conventional SFDI and cSFDI utilize an algebraic demodulation technique referred to as the three-phase method. This method recovers AC intensity from three frames with relative modulation phases of 0, 120, and 240 degrees. A simple algebraic formula (Eq. 1) is applied to these phase-offset images to extract pixel-by-pixel AC information content. It should be noted that only a single spatial frequency is demodulated at a time from these three phases.

$$AC(x,y) = \sqrt{[I_{0^\circ} - I_{120^\circ}]^2 + [I_{120^\circ} - I_{240^\circ}]^2 + [I_{240^\circ} - I_{0^\circ}]^2} \qquad (1)$$

2.2.3 Single Snapshot cSFDI Data Processing

A single raw image is used to simultaneously extract μ_a, μ_s', and SFI. In order to calculate μ_a and μ_s', a Fourier transform is applied line-by-line to raw data to calculate the spatial frequency spectrum of each column vector. This frequency domain data is subdivided into the DC and AC component spectra using top-hat window functions. The cutoff frequency of the window functions was set to 0.11 mm^{-1} and was selected to optimize demodulated image quality specific to our selected spatial frequency. The DC and AC demodulated images are then computed by performing line-by-line inverse Fourier transforms. The process of converting raw data to demodulated DC and AC data is more fully described in Vervandier et al. [33]. The data is calibrated using a phantom with known optical properties to calculate the calibrated diffuse reflectance (step not pictured). The calibration process is outlined extensively in Cuccia et al. [17, 18]. Finally, optical properties are recovered pixel-by-pixel from the DC and AC diffuse reflectance using a Levenberg-Marquardt fit of experimental data to a light-transport model data based on Monte Carlo simulations or the photon diffusion equation [17].

The speckle flow index (SFI) is calculated from the same raw image. Similar to conventional LSI approaches, a 7-pixel x 7-pixel sliding window filter is used to calculate the local spatial standard deviation σ (I) and mean intensity <I>. The ratio of these two components is the speckle contrast (K). Finally, the SFI is calculated pixel-by-pixel according to the equation $SFI=1/(2TK^2)$ where T is the integration time and K is the speckle contrast [29]. SFI is a non-quantitative measurement used as a proxy for relative flow [29].

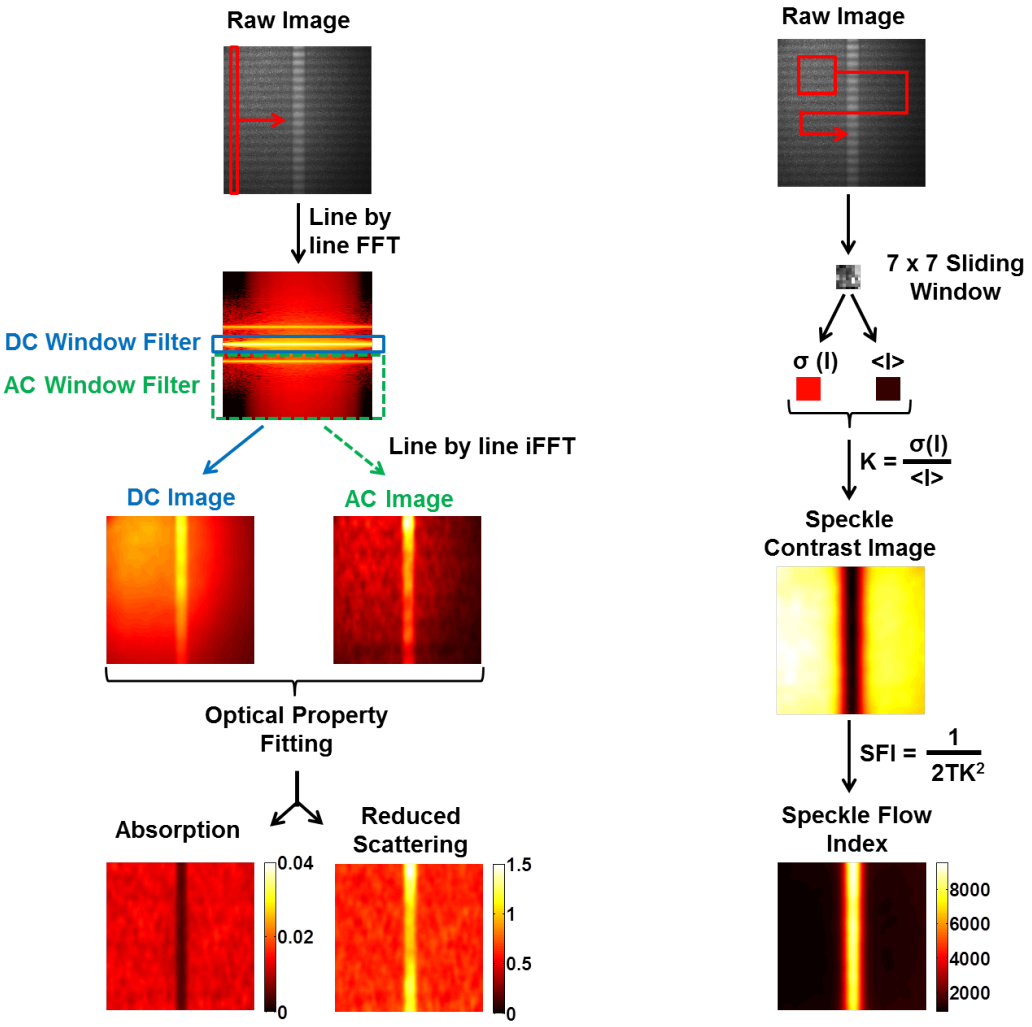

Figure 2.2 Single Snapshot Data flow.Left: Optical properties are calculated from a single raw image of data. The image is Fourier Transformed line-by-line then window-filtered in frequency space. Component spectra are inverse-transformed and calibrated to phantom data to produce DC and AC images. Calibrated data are used to calculate μ_a and μ_s'. Right: Speckle flow index is calculated from the same raw image. A sliding window filter is used to compute the spatial standard deviation and mean intensity. The ratio of these quantities produces the speckle contrast (K) image. Speckle Flow Index (SFI) is then calculated from speckle contrast according to the equation above where T is the integration time.

2.2.4 Homogeneous Phantom Experiments

Homogeneous phantoms were used to validate the ability of single snapshot cSFDI to estimate bulk optical properties by demonstrating agreement with conventional SFDI. Seven

silicone phantoms with unique optical properties were constructed according to Ayers et al. [38]. The μ_a of these phantoms ranged from 0.01 to 0.05 mm^{-1} while μ_s' ranged from 0.5 to 1.5 mm^{-1}. Recovered bulk optical properties were calculated using single snapshot cSFDI and the standard three-phase SFDI technique. μ_a and μ_s' were determined by averaging over a 10 cm x 10 cm region in the center of each phantom. The phantom properties were chosen to demonstrate agreement between single snapshot cSFDI and conventional SFDI. The accuracy, linearity and agreement between SFDI and single snapshot SFDI has already been established over a wide range of optical properties [17, 33]. Due to the non-trivial nature of the phantom making process, the optical properties are not equally spaced.

2.2.5 Flow-Phantom Experiments

A wide-field flow phantom (Figure 2.4) was constructed and used to validate single snapshot cSFDI. More specifically, this experiment was used to evaluate the sensitivity of this technique to changes in flow compared to conventional LSI. The phantom was constructed out of silicone using India ink as the absorbing agent and titanium dioxide as the scattering agent. A 13 mm x 13 mm square acrylic tube was embedded during the curing process to act as a flow channel. The wall thickness of the acrylic was 1.7 mm and the proximal surface of the tube was less than 500 μm beneath the surface of the silicone. The plastic tube was coupled to a syringe pump (New Era Pump Systems) to precisely control the flow speed. During the experiment, the phantom was imaged using both single snapshot cSFDI and conventional LSI while varying the speed of 1% Intralipid from 1 to 5 mm/s in 1 mm/s increments. This range was chosen to reflect red blood cell velocities encountered in microcirculation [39]. Conventional LSI was performed by projecting planar coherent illumination, while single snapshot cSFDI was performed by projecting spatially modulated

coherent illumination. In every other way (aperture, exposure time, optics) the two measurements were completely identical. Fifty sequential frames were acquired at each flow speed. SFI maps were calculated for each frame and averaged over a region of interest that was positioned over the entire length of the tube. Additionally, μ_a and μ_s' maps were recovered from one of the single snapshot cSFDI data sets to demonstrate its ability to recover spatial maps of all three sources of optical contrast.

2.2.6 Forearm Reactive Hyperemia Experiment

An imaging study was performed on the forearm of a healthy subject undergoing a standard reactive hyperemia protocol. During this protocol an automatic inflatable cuff was wrapped around the subject's left upper arm. A full arterial occlusion was applied by inflating the cuff to 210 mmHg. During the imaging study, the volar forearm was imaged at 50 frames per second for 1 minute of baseline, followed by 3 minutes of arterial occlusion, followed by 3 minutes immediately after the release of the occlusion. Each of the 21,000 frames of data was used to reconstruct 2D maps of μ_a, μ_s', and SFI. Regions of interest were analyzed to obtain time course data of μ_a, μ_s' and SFI. Studies here were carried out under the UC Irvine IRB approved protocol, and informed consent was obtained from all subjects (HS# 2011-8370).

2.3 Results

2.3.1 Homogeneous Phantom Experiments

Figure 2.3 shows the results of the homogeneous phantom experiments comparing the optical properties recovered with single snapshot cSFDI and conventional SFDI. The graph at the bottom-left of Figure 2.3 shows absorption recovered with single snapshot cSFDI plotted against absorption recovered using conventional SFDI. Each point corresponds to a

different homogeneous phantom with unique optical properties. The blue horizontal lines are the standard deviation over the region of interest using SFDI, while the red vertical lines are the standard deviation using single snapshot cSFDI. Each error bar in Figure 2.3 is calculated from a single reconstructed image and represents the spatial standard deviation over a 10 cm x 10 cm region of interest as described in Cuccia et al. and Vervandier et al. [17, 33]. The diagonal dashed line is a reference line representing perfect agreement between the two techniques. The average percent difference in μ_a between the two methods was less than 1.2%. On average, the standard deviation of μ_a over the region of interest using SFDI was 0.00083 mm^{-1} while the standard deviation using single snapshot cSFDI was 0.0013 mm^{-1}. The bottom right of Figure 2.3 shows the comparison between bulk μ_s' reconstructed using both methods. Again, each of the points corresponds to a different phantom with unique μ_s'. Due to overlap in μ_s' of some of the phantoms, only five points are shown. The average percent difference between the two methods was 0.59%. The average standard deviation in μ_s' was 0.033 and 0.045 mm^{-1} for conventional SFDI and single snapshot cSFDI, respectively. Overall, these plots of μ_a and μ_s' demonstrate very good agreement in bulk optical property recovery. The images along the top are the reconstructed optical property maps recovered from one of the phantoms using conventional SFDI and single snapshot cSFDI.

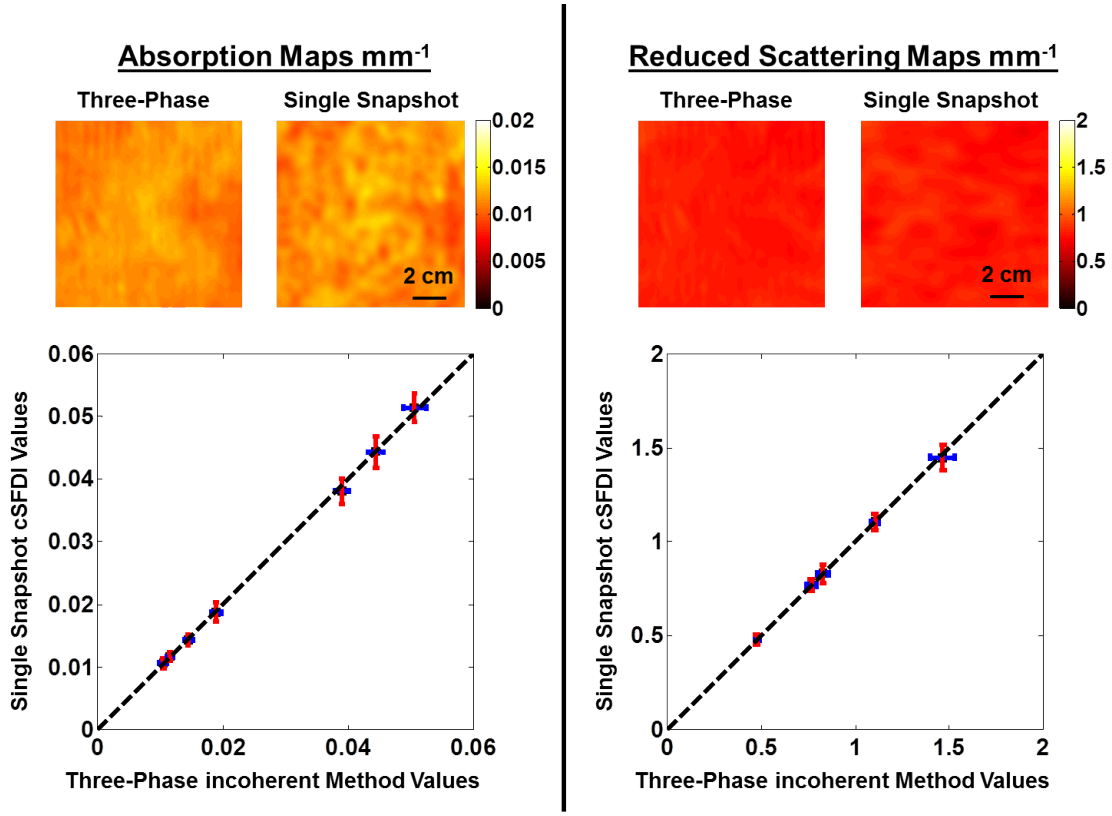

Figure 2.3. Bulk optical property measurements. Left: comparison of bulk absorption reconstruction using standard three-phase SFDI and single snapshot cSFDI. Top two images show absorption maps reconstructed from one phantom using SFDI and single snapshot cSFDI. The bottom plot shows a comparison of bulk absorption between SFDI and single snapshot cSFDI calculated from seven different phantoms. Right: comparison of bulk reduced-scattering reconstruction. The top two images show reduced-scattering maps reconstructed using SFDI and single snapshot cSFDI. The plot at the bottom shows a comparison of bulk reduced-scattering between SFDI and single snapshot cSFDI calculated from five different phantoms.

2.3.2 Flow Phantom Experiment

Figure 2.4 shows a comparison between SFI recovered using modulated AC illumination (single snapshot cSFDI) and planar DC illumination (conventional LSI). Figure 2.4A contains snapshot SFI images of the phantom demonstrating comparable image quality using both methods. Figure 2.4B presents the comparison between SFI recovered with AC (single snapshot cSFDI) and DC (conventional LSI) projections over the area of flow as speed is

increased from 1 to 5 mm/s. Each point corresponds to the SFI at a unique flow speed. These measurements were calculated by averaging over 50 frames of SFI maps. The red error bars represent the standard deviation over the 50 frames calculated from the AC projections while the blue error bars are the standard deviation using DC projections. The dashed line is a trend line fit to these points demonstrating a linear relationship among them. Unlike Figure 2.3, this line is not a "y = x" reference line.

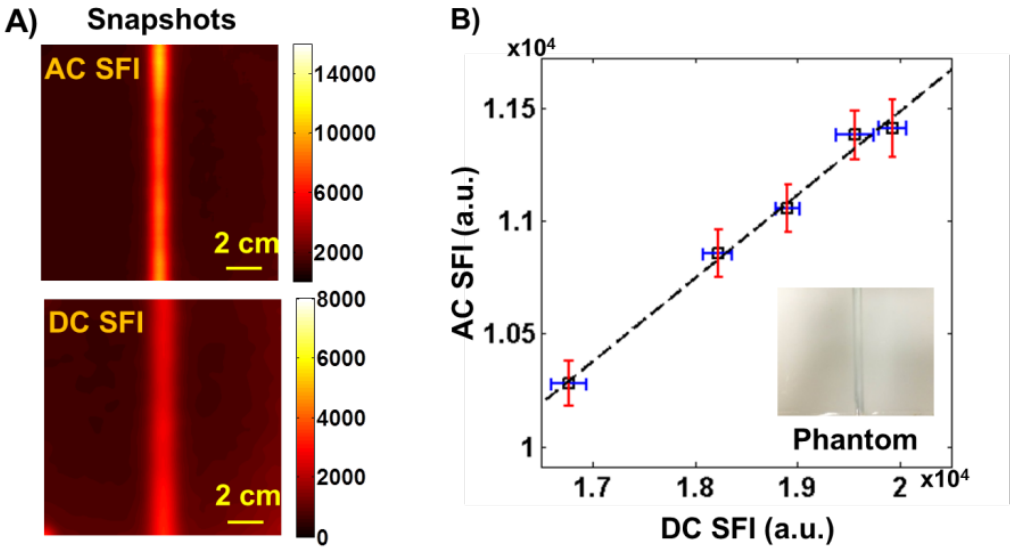

Figure 2.4 SFI measurements. A) SFI images obtained from a flow phantom using spatially modulated AC projections (top) and planar DC projections (bottom). B) SFI values averaged over the region of flow as the speed of the moving liquid is increased from 1 to 5 mm/s in 1 mm/s increments. The graph shows SFI from AC illumination plotted against SFI from DC illumination at each flow speed.

2.3.3 Forearm Reactive Hyperemia Experiment

Figure 2.5 shows the results from the reactive hyperemia experiment. The images across the top of the figure from left to right are the reconstructed μ_a, μ_s', and SFI maps. The plots along the bottom from left to right are the time-series data for μ_a, μ_s', and SFI. The red and blue curves in the time-series data are derived from the correspondingly-colored red and blue regions of interest (ROI) overlaid on the property maps. Both ROIs were chosen by

visually assessing the absorption image in Figure 2.5. The blue ROI was placed over an area with a subcutaneous vein, while the red ROI was placed over an area without one. The time-series data also indicate when the occlusion and release of the pressure cuff occurred. During the occlusion, there was a 32% increase in absorption in the blue channel and a 71% increase in the red ROI. These increases in μ_a were gradual and corresponded primarily to the accumulation of deoxyhemoglobin during the occlusion. Following the release there was a 43% decrease in μ_a in the blue ROI and a 72% decrease in the red ROI. This decrease occurred in less than 25 seconds and was caused by the reperfusion of oxyhemoglobin and the washout of deoxyhemoglobin. SFI showed a decrease of 51% in the red ROI and 28% in the blue ROI during the occlusion. After the release, there was a 190% increase in the red ROI and a 146% increase in the blue ROI. These large increases occurred over the course of 10 seconds indicating the immediate return of flow to the forearm. Changes in μ_s' are also seen during the occlusion and release portion of the experiment. However, these variations were significantly smaller than those witnessed in μ_a and SFI. Elucidating the nature and significance of these slight variations is left to future studies.

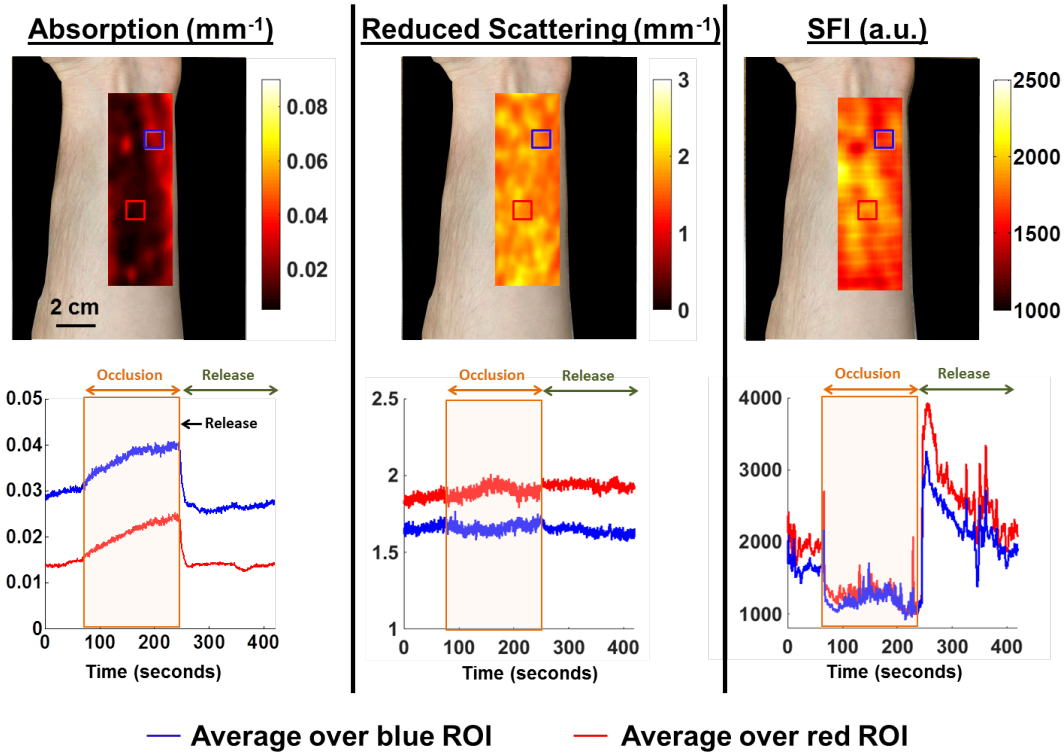

Figure 2.5 *In vivo* forearm reactive hyperemia experiment. Top from left to right: spatial maps of absorption, reduced-scattering, and speckle flow index. Bottom from left to right: time-series data of absorption, reduced-scattering and speckle flow index from the two regions of interest in the images. A 660 nm laser diode was used in this experiment.

Figure 2.6 demonstrates the ability of single snapshot cSFDI to detect the heartbeat waveform within the SFI at multiple regions of interest within the field of view. Figure 2.6a shows one frame from the recovered SFI map overlaid on the subject's forearm during the reactive hyperemia protocol. The black and blue regions of interest correspond to the black and blue time-series data within the rest of Figure 2.6. Figure 2.6b shows the entire cuff-occlusion-release time-series data. The brown shaded region lies over the occlusion segment while the green shaded region lies over the release of the occlusion. These data both demonstrate sensitivity to reactive hyperemia signified by the increase in SFI following the occlusion. Figure 2.6c shows the frequency spectrum of the blue curve in Figure 2.6b for the

segment during the occlusion (brown box) and the release (green box). The peak in the release at 1.2 Hz corresponds to the heartbeat signal (72 beats per minute). These spectra demonstrate the presence of the heartbeat component during the release that is absent during the occlusion due to the upstream arterial blockade of blood flow. This is confirmed intuitively by Figure 2.6d which shows zoomed-in plots of both curves during 30 seconds of the occlusion and 30 seconds of the release. Note the periodic signal that is present during the release. Upon close inspection it is apparent that these two curves (black and blue) are both of the same frequency and phase over the entire duration. In contrast the segment from the occlusion data is more chaotic and lacks a clear periodic signal. Finally, Figure 2.6e shows an even more zoomed-in view of the release segment, revealing a more detailed look at the heartbeat. Here it is possible to see structure within the signal during each heartbeat. These features could possibly contain information about the vasculature such as the dicrotic notch and reflections within the arterial tree. The spacing of the peaks was analyzed and shown to be at 1.2 Hz, in agreement with the Fourier analysis.

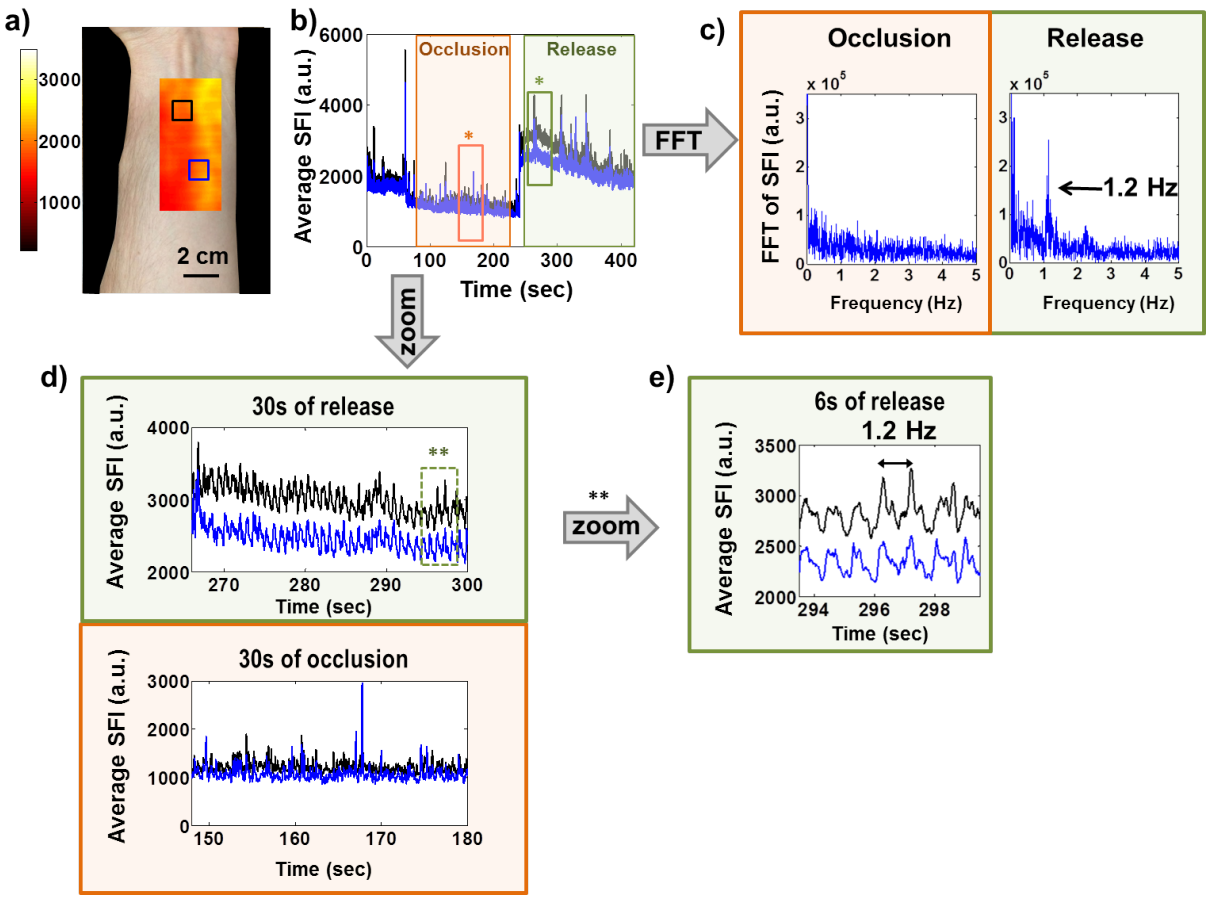

Figure 2.6 Dynamic response to post occlusive reactive hyperemia a) Image of the subject's forearm with overlaid SFI map. b) Time series SFI data from blue and black regions of interest during the cuff-occlusion-release protocol. The light-brown shaded box corresponds to the occlusion portion of the experiment, while the light-green shaded box corresponds to the release of the occlusion. c) Fourier transforms from the occlusion (light-brown) and the release (light-green). d) 30 second zoomed-in intervals taken from the occlusion and release portions of the data. The green shaded box corresponds to the green rectangle with the asterisk in fig. 6b. The brown shaded box is a zoomed in interval from the brown rectangle with the asterisk in fig. 6b. e) An even closer look at the signal during the release. These data correspond to the green rectangle with two asterisks (**) in figure 6d.

2.4 Discussion

In this work we introduce a noncontact noninvasive imaging technique capable of extracting μ_a, μ_s', and SFI in real-time (50 fps) over large (15 x 15 cm) tissue regions. By

applying advanced processing techniques to single raw images of spatially modulated coherent light, we are able to calculate optical properties from a single frame of data. Additionally, speckle contrast can be extracted from the same image because of its coherent properties. Needing only a single frame of data allows for simplified hardware; a fixed object such as a sinusoidal-patterned slide can be used in place of a DMD or LCOS projector in the case of conventional SFDI.

Homogeneous phantom experiments demonstrate that single snapshot cSFDI can be used to recover accurate optical properties over large ranges of absorption and reduced-scattering when compared with conventional 3-phase SFDI using an incoherent light source. Flow phantom experiments show that single snapshot cSFDI has comparable sensitivity to LSI in terms of measuring dynamic scatterer flow speeds. These same experiments also demonstrate the ability of single snapshot cSFDI to extract all three contrast mechanisms from a single frame of raw data. Access to this information enables the correction of speckle contrast for optical properties. In addition, an advantage to calculating speckle contrast from an AC projection is that it is possible to achieve higher speckle contrast values by rejecting long path-length photons [21, 24]. This is why in Figure 2.4 the SFI is lower for the AC modulation pattern; SFI is inversely proportional to speckle contrast, and speckle contrast from an AC projection is higher than the corresponding DC illumination. This potentially enables more accurate characterization of superficial microcirculation.

In vivo studies of reactive hyperemia demonstrate the ability of single snapshot cSFDI to measure intrinsic signals relevant to dynamic physiology. During the occlusion we observed increases in μ_a at 660 nm indicative of a buildup of deoxyhemoglobin. Following

the release of the occlusion we observe a sharp decrease in μ_a signifying the washout of deoxyhemoglobin as oxyhemoglobin re-entered the tissue compartment. The increase in SFI above baseline observed after the occlusion demonstrates sensitivity to post occlusive reactive hyperemia, a well-established physiological phenomenon.

Beyond demonstrating sensitivity to dynamic physiological processes, these *in vivo* measurements point to the potential of single snapshot cSFDI to measure the tissue metabolic rate of oxygen consumption. The current system presented in this paper has only a single optical wavelength and is therefore only capable of extracting tissue absorption and scattering coefficients. However, by extending this system to multiple wavelengths it would have the ability to decouple the chromophore concentrations of oxy- and deoxyhemoglobin ([HbO_2] and [HHb], respectively). Combining blood hemoglobin concentrations with flow measurements can be used to generate an index for oxygen consumption in accordance with Fick's principle. Measuring the metabolic rate of oxygen consumption has multiple potential applications and can provide important insight into pathologic conditions where flow and metabolism are uncoupled. For example, oxygen utilization is known to be decreased in conditions of chronic hypoxia caused by prolonged arterial occlusion, such as peripheral arterial disease (PAD). Real-time measurements could provide clinicians with important information relevant to early diagnosis, disease staging, and treatment response monitoring.

The ability to extract spatial maps of multiple contrast sources in real-time has numerous potential benefits outside of oxygen metabolism. In this work we were able to observe the heartbeat in the SFI channel. Characterization of the heartbeat waveform has potential to unlock information related to arterial stiffness and blood pressure [40, 41]. By

observing the heartbeat over large tissue areas, it may be possible to directly observe pulse transit time by measuring how the waveform changes in phase over areas of tissue. In this work we performed imaging using a 660 nm laser diode, a wavelength with greater sensitivity to deoxyhemoglobin than oxyhemoglobin. By performing single snapshot cSFDI with a wavelength with greater HbO_2 sensitivity (e.g. 850 nm) there is potential to measure the plethysmographic waveform in the absorption or DC reflectance data. In this case, single snapshot cSFDI would be able to measure the heartbeat simultaneously in absorption and SFI, and potentially be used to look at shifts in phase associated with intrinsic physiology.

Beyond physiology, mapping multiple contrast sources has the potential to improve quantitative accuracy of SFI. Previous work has demonstrated that speckle contrast is dependent on tissue optical properties and the sampling volume. Changes in the absorption and reduced scattering coefficients were shown to change speckle contrast for a given flow speed. Likewise, the depth at which flow occurs also affects the speckle contrast recovered at a given flow speed. Single snapshot cSFDI has the ability to correct for both of these effects. An optical property alteration algorithm, based on Monte-Carlo simulations of light transport, can take into account the optical properties recovered using single snapshot cSFDI to adjust the speckle contrast, and thus SFI values. Additionally, speckle contrast calculated in the spatial frequency domain can be used to control for the measurement depth. Together, these effects can be used to improve quantitative accuracy of the speckle contrast measurements in single snapshot cSFDI [21, 24].

In summary the information rich spatiotemporal data set recovered by single snapshot cSFDI has significant potential. By combining blood concentrations with blood flow speed

there is the possibility to measure chromophore concentrations. Measuring the heartbeat in the absorption parameter and speckle contrast channels may reveal physiologically relevant information about microcirculatory physiology. Finally, single snapshot cSFDI offers the potential to improve quantitative accuracy of speckle information by controlling for optical properties and measurement volume. In future work, this system will be extended to multiple wavelengths to measure chromophores then transformed into a portable clinic-ready device suitable for *in vivo* physiological measurements.

CHAPTER 3 NONINVASIVE HEMODYNAMIC CHARACTERIZATION USING AFFIXED TRANSMISSION SPECKLE ANALYSIS

3.1 Introduction

In this chapter we address a different coherent light technique referred to as Affixed Transmission Speckle Analysis (ATSA). ATSA consists of a single coherent light source and CMOS detector which obtains single point measurements from a subject's digit e.g. finger or toe. By collecting data at high speeds, ATSA is capable of recreating the pulsatile waveform from the heartbeat.

3.1.1 Affixed Transmission Speckle Analysis

Noninvasive hemodynamic assessment refers to techniques used throughout medicine to characterize the cardiovascular system. Notable examples include Photoplethysmography (PPG), Doppler ultrasonography, and electrocardiography. In the context of peripheral arterial disease, hemodynamic assessment could provide information about arterial deterioration; several PPG studies have shown waveform changes associated with atherosclerosis [42]. In many ways PPG is an ideal monitor: it is inexpensive, noninvasive, and embedded in a convenient clip-on form factor. However, PPG suffers from low signal to noise especially in patients with decreased perfusion.

Coherent light detection offers a novel method for the peripheral measurement of the cardiac waveform. Recently, a spin-off group from BLI produced a clip-on instrument capable of monitoring the cardiac waveform in multiple contrast mechanisms. This device is referred to as Affixed Transmission Speckle Analysis (ATSA) and consists of miniaturized LSI in transmission geometry that can be clipped onto a digit. The principle behind this device is that from a single coherent light source it is possible to extract two signals, one

derived from speckle decorrelation and one derived from light intensity. Because the camera is run at approximately 200 Hz, this device is capable of measuring heartbeat pulsatility in both signals. The speckle derived waveform is referred to as the Speckleplethysmogram (SPG) and the intensity-based waveform (like that obtained with an incoherent source) is the PPG. Although these two signals are measuring the heartbeat, they probe different aspects of the underlying tissue physiology. The SPG is sensitive to the pulsatile blood flow and the PPG is sensitive to pulsatile vascular volume.

The combined SPG-PPG signal provides a unique fingerprint of the vasculature. Pulsatile waveforms originating at the heart propagate through the arterial network. Along the way, these pulsatile waveforms – manifesting in pressure, velocity and elastic expansion – are directly related to the underlying mechanical properties through which the signals propagate. Therefore, these pulsatile signals, containing rich information related to the state of the vasculature, can potentially be used as a way of characterizing the physical properties of the underlying health of the system.

In this chapter we present several methods for extracting physiological data from the SPG-PPG signal. We begin by demonstrating the process by which the SPG and PPG can be extracted from the same raw data obtained using a single coherent light source, and we provide the physiological mechanism responsible for each signal. We proceed to show that the signals are offset in nature and propose a method that quantifies this timing offset. We also propose a method that measures frequency content embedded in the SPG alone. Next, both signal decomposition strategies (time-delay and frequency content) are applied to *in vivo* measurements. We demonstrate that there are strong correlations between age and time-delay, and between age and harmonic content. Finally, we demonstrate changes in

time-delay in response to exercise and cold-pressor challenges. Overall this data demonstrates a relationship between the SPG-PPG signal and arterial compliance and vascular tone.

3.2 Methods

3.2.1 Instrumentation

ATSA consists of miniaturized LSI technology in compact finger-clip form factor set in transmission geometry. ATSA takes advantage of speckle signals that have penetrated the skin at least several millimeters. The light source consists of a 785 nm laser diode while the detector consists of a CMOS detector. The source and detector are placed opposite one another in a form factor similar to a commercially available pulse-oximeter.

3.2.2 Theory

Figure 3.7 shows how the SPG and PPG signals are extracted from raw data. Within the ATSA device there is a 785 nm laser diode placed opposite to a CMOS camera. The camera acquires images of the speckle interference pattern at approximately 200 frames per second. On a frame-by-frame basis, a 7 x 7 pixel sliding window filter is used to extract the mean intensity <I> and the standard deviation <σ> of the raw images. This data is then used to construct the average intensity matrix and the speckle contrast (K) matrix, consisting of the ratio of the standard deviation and mean intensity. At this point the average intensity array is input into the standard PPG equation $1/Log(< I >)$ [28, 43], producing the PPG array. The average of the entire PPG array yields to the single PPG time point. At the same time the speckle contrast is used to produce the SPG array using the equation shown in Figure **3.7**. This equation has been validated experimentally to produce a number that is linear with volumetric flow and often referred to as the speckle flow index

[39]. Finally, this array is averaged to produce a single SPG time point. This process is repeated for every frame acquired at 200 frames per second and is used to construct the SPG and PPG time-series, both from the same raw data arrays.

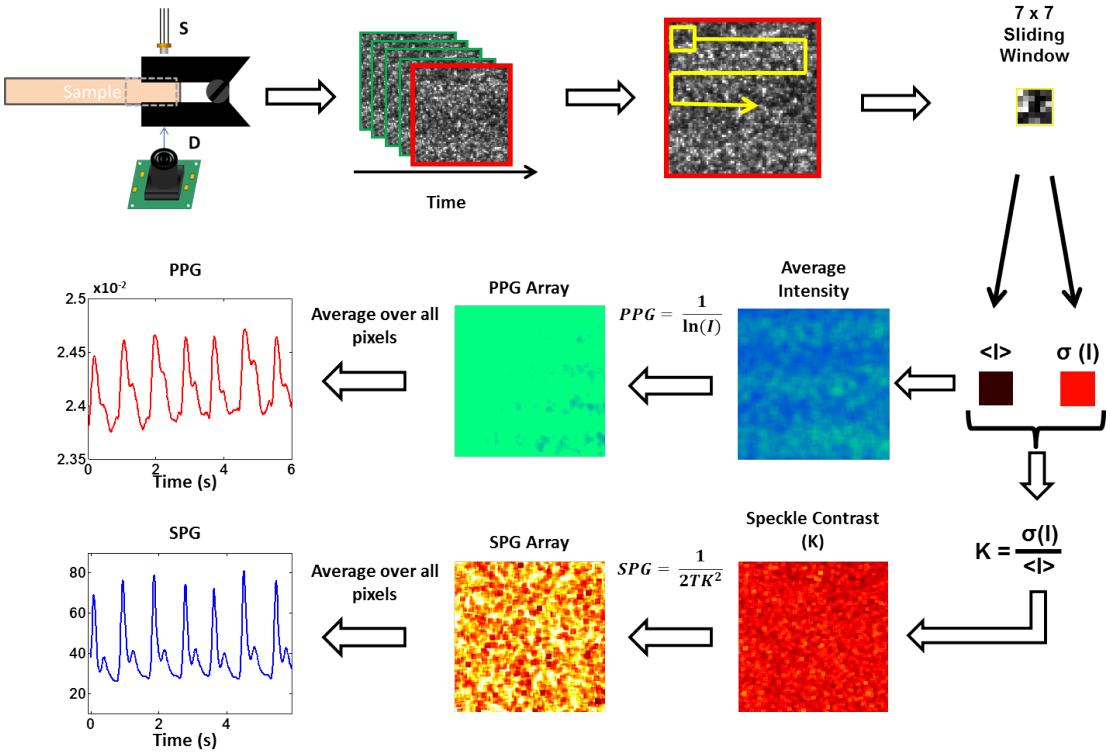

Figure 3.7 SPG-PPG Signal Processing. Within the ATSA device a 785 nm laser diode and on-chip CMOS camera sit in transmission geometry. The transmission laser speckle pattern is picked up by the camera in at a rate of approximately 200 frames per second. Each individual image (speckle interference pattern) is processed individually. A 7x7 sliding window filter is used to extract the standard deviation and mean intensity images. The average intensity from the sliding filter is used to assemble the "Average Intensity" array, while the speckle contrast (K) array is assembled from the ratio of standard deviation over intensity (σ(I)/<I>). The PPG array is computed pixel by pixel from the Average Intensity array according to the equation 1/(ln(I)), where ln is the natural logarithm and I is the intensity. Averaging over the entire PPG array provides an individual point in time on the PPG time tracing. Each point comes from a different captured image. The SPG array is computed from the from the speckle contrast (K) according to the equation $1/(2TK^2)$ where T is the detector integration time and K is the speckle contrast. The entire speckle contrast array is averaged over in order to produce a single point in time on the SPG tracing.

Figure 3.2 demonstrates how the SPG-PPG signals are related to vascular physiology. The sample, typically a digit on the subject's hands or feet, is placed within the finger clip such that it falls between the light source and detector (Figure 3.2, top-left). Light from the coherent source enters the tissue and is scattered randomly by a combination of static and dynamic scatterers [44, 45]. Static scatterers are comprised of matrix materials (e.g. collagen) and membranes belonging to stationary cells and organelles [45]. Dynamic scatterers consist of the membranes belonging to moving red blood cells [44]. Light passing through the tissue is also heavily attenuated by absorbers contained in the tissue; the most important of these is hemoglobin, the oxygen-transporting molecule confined in the cytoplasm of red blood cells [45]. Dynamic scattering modulates light coherence producing the SPG signal. Likewise, attenuation due to absorbers modulates light intensity producing the PPG signal. It is well established that blood pressure is pulsatile within the arteries and arterioles, but loses pulsatility once it has reached the capillary bed and down-stream in the venous plexus [46]. Therefore, pulsatility either in attenuation or coherence is coming from the arterial side of the vasculature. Pulsatility in the SPG is due to variation in dynamic scattering due to changes in volumetric flow, whereas pulsatility in the PPG is due to variation in the concentration of absorbers caused by vessel expansion [47]. It can be seen then that two pulsatile signals, originating from different light properties, are caused by two separate physiological processes.

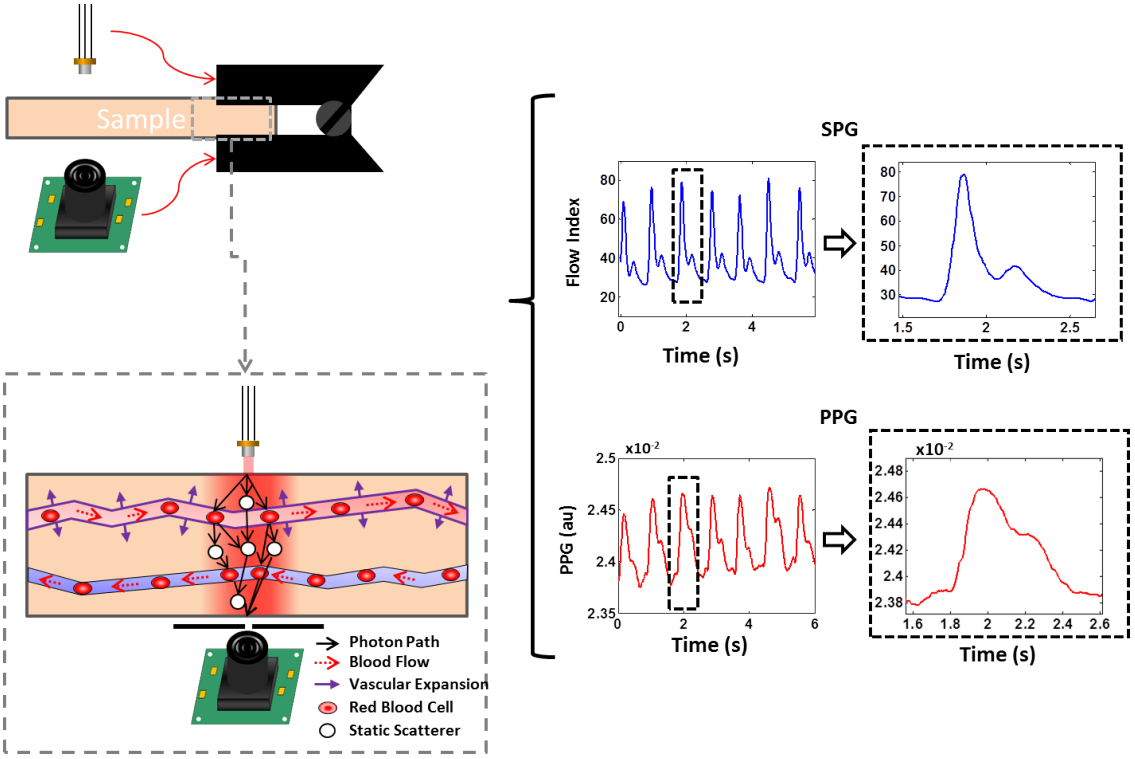

Figure 3.8 ATSA Instrument Description. The top left of the figure shows a schematic of the ATSA finger clip device affixed to a sample. A laser diode and on-chip CMOS camera are installed within the housing on opposite sides of the sample, such that light coming from the diode transmits through the sample prior to interacting with the camera. The bottom left shows demonstrate the light-tissue interaction taking place in ATSA. Coherent light from the laser diode is enters the sample and undergoes absorption and static and dynamic scattering. Some of this light reaches the pinhole aperture camera on the opposite side and creates a constructive and destructive interference pattern on the detector known as speckle. Movement of the red blood cells causes blurring of the interference pattern which can mathematically be transformed into a metric for blood flow called the Speckle Flow Index. The pulsatile nature of blood flow picked up in the SFI Index yield the Speckle Plethysmogram (SPG). Simultaneously, fluctuations in the arterial input causes the vessels on the arterial side to expand and contract dynamically with the cardiac waveform, leading to fluctuating intensity on the detector caused by time dependent changes in total absorption from hemoglobin. These changes in intensity on the detector produce the Photoplethysmogram (PPG).

3.2.3 Data Processing Procedures

In this work we present two SPG-PPG processing methodologies. Figure 3.3 graphically shows how time-delay (TD) is calculated. The systolic peak is located on a beat-by-beat basis for both the SPG and PPG signals. This is done automatically using a basic peak finding algorithm available in many computational software packages, or by selecting them by hand. The TD is then calculated by subtracting the SPG peak time from the PPG peak time for every heartbeat in the data set. The average is then taken over many heartbeat cycles; in this work the average is taken from at least 120 heartbeats.

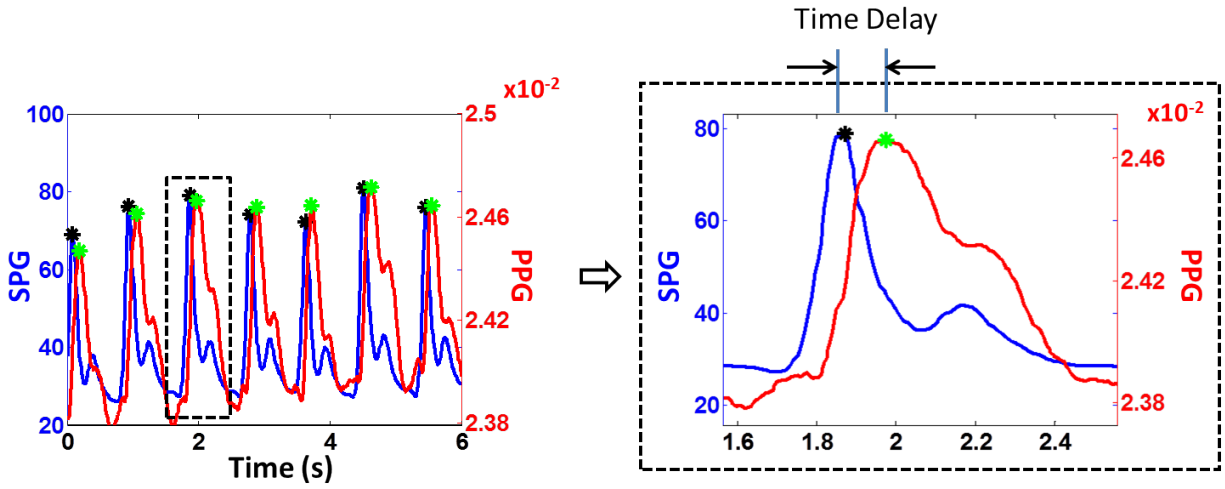

Figure 3.9 Calculation of Time Delay. The left panel shows the SPG and PPG in blue and red, respectively. The right panel shows a close-up of a single cardiac cycle. The time-delay between the two signals can be calculated by locating the peaks and then subtracting their locations in time. This process is then repeated for the next cardiac cycle.

Figure 4 graphically shows the SPG harmonic content extraction process. In this procedure, a single heartbeat is isolated from the SPG time-series. The pulse is appended to itself 1000 times then Fourier transformed to produce a harmonic spectrum: a spectrum of discrete peaks corresponding to the harmonics of the data. Finally, the height of each

discrete peak is determined and used to produce harmonic ratios. These ratios are stored in an array and then the process is repeated for the next heartbeat in the time-series. An average is taken to produce a single measurement for each ratio. In this work we focus our analysis on the third harmonic ratio: H3 / H1 as shown in Figure 3.10.

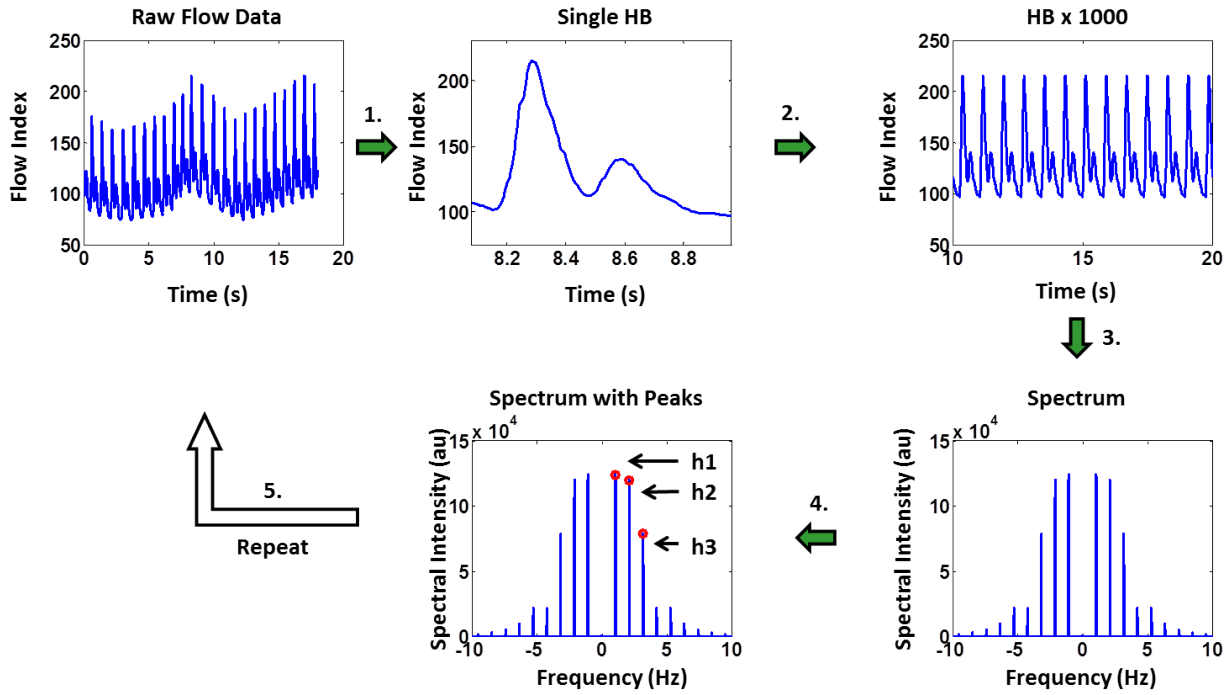

Figure 3.10: Time Frequency Analysis. The top left shows a raw SPG tracing from which (1) a single cardiac waveform is extracted. (2) This waveform is then appended front-to-end 1000 times to create a long series of identical waveforms. (3) The FFT of the 1000 waveform series is computed to yield the frequency spectrum, consisting of distinct harmonic peaks. (4) The heights of each harmonic are then used to calculate harmonic ratios, discrete values stored for each cardiac cycle. (5) The method repeats for the next cardiac cycle, accumulating harmonic ratios into a distribution that can be visualized with a histogram or used to compute a mean.

3.2.4 Post-Occlusive Reactive Hyperemia

Post-occlusive reactive hyperemia (PORH) consists of occluding a subject's upper arm for 3 to 5 minutes using a pneumatic cuff pressurized to 215 mmHg to occlude the brachial artery [48, 49]. The occlusion leads to a buildup of metabolic byproducts that vasodilate

the arm such that when the occlusion is released blood flow is significantly higher than at baseline. In summary, PORH is a state of decreased arterial constriction which leads to increased blood flow in the occluded extremity. In this experiment the cuff occlusion was used to enhance the PPG by increasing vasodilation. It should be noted that PORH was not used for its usual intended purpose of comparing the hyperemic state to baseline measurements for measuring endothelial function [50].

3.2.5 Cold Pressor Challenge

The cold pressor challenge consists of challenge consists of the subject submerging one hand in ice water for 30 seconds to a minute causing peripheral vasoconstriction along with a slight increase in heart rate and blood pressure [51]. In this work, the ATSA device was attached to the subject's left index finger while a baseline measurement was acquired for 2 to 3 minutes. At this point the subject inserted his opposite hand (right hand in this case) into the ice water for as long as he was able to tolerate – usually 30 to 90 seconds – all while data continued to be acquired on the non-submerged hand. This data was processed to calculate TD. In order to assess repeatability, this process was repeated on one subject 7 times. In order to assess the effects in general, this test was performed on 5 subjects aged 25 – 35; there were 4 males and 1 female.

3.2.6 Exercise Challenge

The exercise challenge consisted of the subject performing 10 minutes of cardiovascular exercise on a stationary bicycle. The subject's left index finger was measured with the ATSA for 2 minutes before and 2 minutes following the challenge. Cardiovascular exercise is known to decrease peripheral vasoconstriction especially in the superficial vascular beds [52]. It also increases blood pressure and cardiac output by increasing the heart rate and

stroke volume. The decreased peripheral vasoconstriction is required to vent excess heat and the increased cardiac output is necessary to supply working muscle with oxygen and nutrients needed for heightened metabolic activity.

3.3 Results

3.3.1 Change in Time-Delay and Harmonic Content observed with age

Figure 3.11 shows the time-delay results for two subjects calculated from the 300-second interval following the release of the arterial occlusion. Subject A is a 71-year-old female with known cardiovascular risk factors including a history of smoking, hyperlipidemia, hypertension and type-2 diabetes. Subject B is a 23-year-old male with no known significant cardiovascular risk. These two subjects were chosen as an archetypal example of how time-delay can vary among patients. The left graph is a double-axis plot of a 4-second period of SPG (blue) and PPG (red) for subject A, while the middle graph shows the same double-axis plot for subject B. The black asterisks show the peak maxima of the SPG and the green asterisks show the peak maxima for the PPG. It can be seen from these plots that the PPG for subject A is broader than that of subject B, who has a much more pronounced PPG peak. Additionally, subject A's PPG more closely resembles the SPG curve. Subject A on the other hand does not have such a clearly defined PPG peak, and qualitatively the PPG does not resemble the SPG as closely. These signal characteristics seem to account for the longer time-delay extracted from subject A than subject B. The histogram on the right side of the figure shows the distributions of time-delays from each subject; subject A has both a greater time-delay as well a wider distribution.

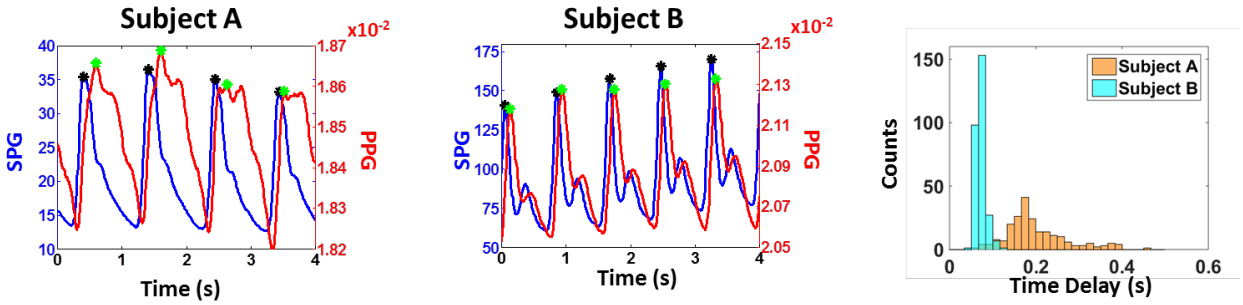

Figure 3.11 Two-Subject Comparison of Time Delay. The left graph shows the double axis plot of SPG and PPG marked in blue and red, respectively, for subject A. The middle graph shows the double axis plot for Subject B. The SPG and PPG peaks are highlighted with black and green asterisks, respectively. The histogram on the right shows the distribution of time delays for both subjects.

Figure 3.12 shows the harmonic content results for the same two subjects calculated from the 300-second time interval following the release of the arterial cuff-occlusion. The third harmonic ratio (THR), which is the ratio of the third harmonic to the first harmonic (fundamental), was used in this example. The top-left and bottom-left plots present a single heartbeat SPG waveform extracted from subject A and subject B, respectively. Qualitatively, Subject B contains more structure than subject A as evidenced by the presence of a secondary reflection. The plots to the right of the single heartbeats are the respective frequency transforms. The THR consisted of the ratio of the third peak to the first peak. The histogram on the right of Figure 3.12 shows the THR distributions for both subjects, demonstrating that subject B has a higher mean THR and a broader spread than subject A. In other words, the older subject had less harmonic content in terms of the THR, and a more repetitive structure as evidenced by there being less variation in the THR.

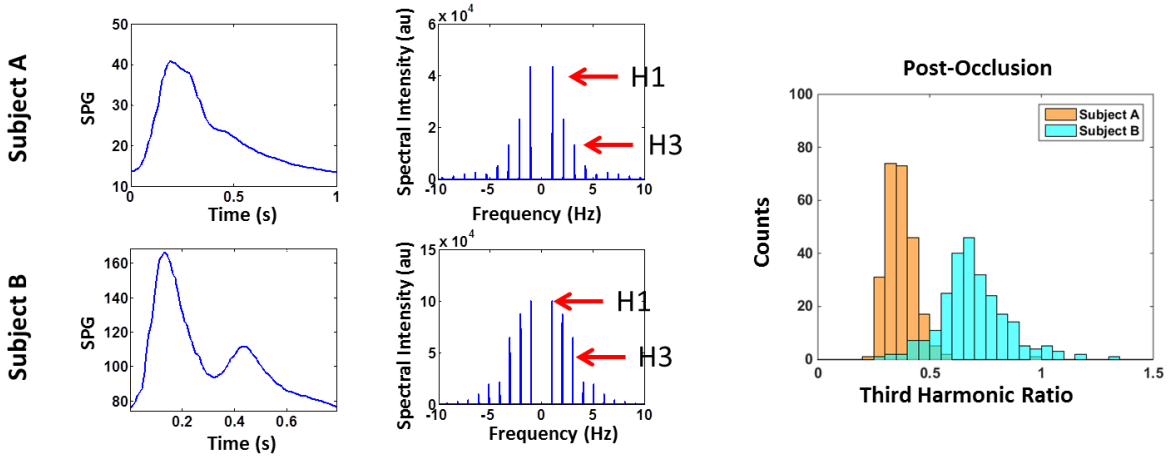

Figure 3.12 Two-Subject Time Frequency Analysis Comparison. The top left graph shows a single cardiac cycle extracted from the raw flow data of subject A. To the right of this is the frequency spectrum computed for this waveform where H1 and H2 demarcate the first (fundamental) and second harmonic. Directly below these are the two counterpart graphs for subject B. The histogram on the right shows the distributions of the harmonic ratio (H2/H1) for subjects A and B for all waveforms available in the raw data.

Figure 3.11 and Figure **3.12** together demonstrate the differences between two archetypal extremes: the young healthy subject has a shorter time-delay and more harmonic content than the older subject with significant cardiovascular risk factors. This is meant as a preliminary example of the possibilities with this new device, not as significant proof of its efficacy in risk stratification.

Figure 3.13 presents time-delay regressed onto subject age (Figure 3.13a) and THR regressed onto subject age (Figure 3.13b). The solid red lines indicate the best linear fit, the dotted red lines show the 95% confidence intervals, and the blue tick-marks show the individual subject data. All data-points were calculated from raw data that followed the release of the arterial cuff occlusion as described in the methods section. The adjusted R^2 for the regression of time delay onto age and THR onto age were 0.69 and 0.538, respectively. For the regression of time delay onto age, the p-value was 4.5×10^{-5}; this is an

evaluation of significance of the regression versus a constant model. In other words, this p-value describes the probability that the data lacked any trend or the probability that the time delay does not change with age. The p-value of the regression of THR on age was 0.000735. Overall these data indicate that there is a significant trend associated with age for both parameters.

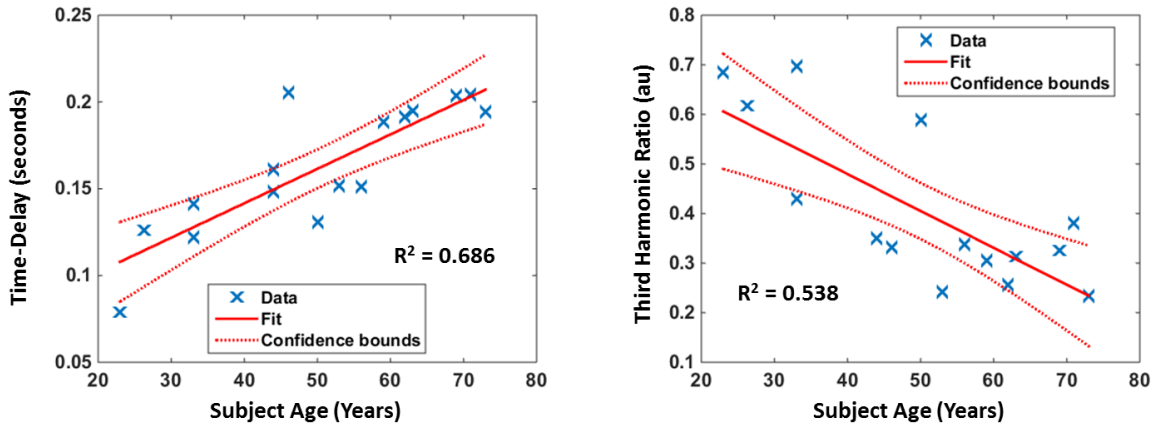

Figure 3.13: Regression of SPG-PPG Parameters onto Age. 7a: Regression of SPG-PPG time delay onto age. 7b: Regression of Third Harmonic Ratio onto age.

3.3.2 Cold Pressor Exercise Challenge

Figure 3.14 shows one example of data from the cold pressor challenge. This was taken from a 29-year-old subject in good health. The plot on the left shows a double-axis plot of the SPG (blue) and the PPG (red) during 5 seconds of the 2-minute baseline measurement. The plot in the middle shows is the same for 5 seconds during the cold-pressor challenge. The PPG in this example is more rounded than the baseline pulse; the systolic upshot in the PPG visually is steeper at baseline. This observation seems to explain why the time-delay is increased in the cold condition. It is also noteworthy that systolic upshot in the SPG (blue) seems to retain its steep slope in both baseline and cold conditions.

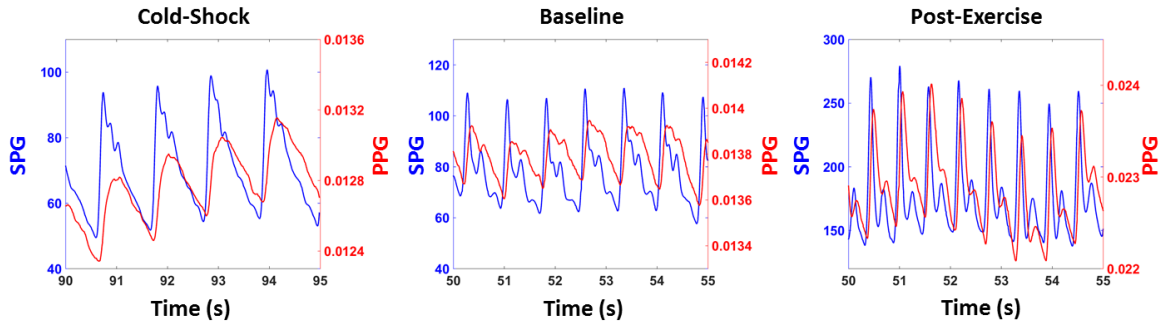

Figure 3.14 Cold Shock and Post-Exercise SPG-PPG Data. The left plot shows data from the cold shock, the center plot shows a baseline tracing, and the right plot shows post-exercise.

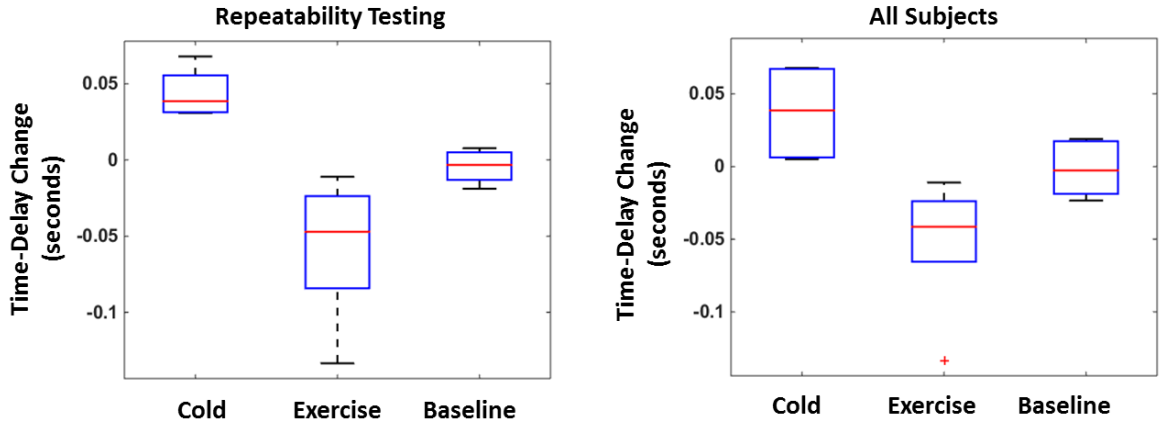

Figure 3.15 Summary of Results from Cold-Pressor and Exercise Challenges.

Figure 3.15a summarizes the repeatability testing on a single subject performing the exercise and cold-pressor challenges. Each box is intended to show how time-delay changes from baseline for each challenge. The box labeled “baseline” consists of how time-delay changed in two sequential baseline measurements. The average increase in TD for the cold challenge was found to be 0.044 seconds, with a range of 0.031 to 0.068 seconds. The average change in TD for the exercise challenge was found to be -0.0578 seconds, with a range of - 0.0110 to - 0.1334 seconds. The difference between the cold and exercise distribution was found to be a significant with p = 0.0013. The difference between the cold

and baseline distribution was found to be significant with p = 0.0031. The difference between exercise and baseline distributions was found to be significant with p = 0.0286.

This description has been included to clarify the measurements in Figure 3.15a. The box-plot on the left shows repeatability testing within a single individual. Each box contains 7 repetitions. For the box marked cold, each of the seven measurements consists of the average time delay calculated at baseline subtracted *from* the average time delay calculated during cold-shock ($TD_{cold} - TD_{baseline}$). Similarly, the box marked exercise contains seven measurements of baseline subtracted from post-exercise ($TD_{post\text{-}exercise} - TD_{baseline}$). Finally, the box marked baseline is derived from two sequential baseline measurements – one subtracted from the other ($TD_{baseline\ 1} - TD_{baseline\ 2}$). The measurements were taken in this way to emphasize sensitivity to the change associated with exercise and cold, and to minimize the effect of variability of the actual values of TD among different measurements.

Figure 3.9b summarizes the results from several individuals performing the exercise and cold-pressor challenges. As in figure 3.9a, each box shows how TD changes from baseline for each of the challenge among the individuals. The box labeled “baseline” is the difference between paired 2-minute baseline measurements. The average increase in TD for the cold challenge was found to be 0.0294 seconds, with a range of 0.0051 to 0.0671 second. The average decrease in TD for the exercise challenge was found to be 0.0430 seconds, with a range of 0.0238 to 0.0654 seconds.

3.4 Discussion

This work introduces methods for extracting physiological parameters from the SPG-PPG signal obtained with ATSA. We demonstrate how the dual SPG-PPG signal is derived from the same raw data obtained with an instrument consisting of a CMOS camera and

coherent light source with the SPG originating from flow pulsatility and the PPG originating from volumetric pulsatility. We demonstrate that both waveforms are offset in time and introduce an algorithm characterizing time delay between the systolic peaks. Additionally, we introduce a framework for analyzing SPG structure by calculating harmonic content on a pulse-by-pulse basis. Two signal decomposition methods (time delay and harmonic content) are applied to *in vivo* measurements to demonstrate physiological significance, with our analysis revealing age correlations for both. We proceed to demonstrate changes in time delay associated with exercise (decreased time delay) and cold pressor challenges (increased time delay).

The correlation between age and extracted SPG-PPG parameters suggest that these methods are sensitive to arterial stiffness and vascular aging. Aging arteries undergo mechanical changes resulting in decreased compliance, referred to as arterial stiffening. Thus, the correlations between SPG-PPG parameters and age indicate potential sensitivity to these mechanical changes. This implies SPG-PPG analysis may be used for noninvasive vascular assessment at early ages as a predictive measure of arterial health outcomes. We observe that the age-related time delay increases are due to pulse-shape changes in the PPG caused by decreased arterial compliance. In fact, these changes in PPG shape have been previously observed in the field as an increase in crest time [47, 53]. Our work presents this phenomenon in a new light using the SPG as the reference signal, rather than relying on the PPG which is often subject to artifacts and low signal to noise ratio [54, 55]. The mechanism for changes in SPG signal and harmonic content comes from a distinct aspect of vascular physiology. Refractive index mismatch at vessel bifurcations increases with atherosclerosis [42]. This results in the reflection of high-frequency harmonic

components as the pulse propagates down the arterial network explaining why there is less harmonic content seen in the older individuals in this study. Our analysis methods could potentiate a noninvasive means of characterizing vascular age for cardiovascular risk stratification. Additionally, it could be applied to early detection of atherosclerosis for early medical and lifestyle interventions.

The changes in time-delay caused by cold pressor and exercise challenges indicate a completely different functionality related to vascular tone. Vascular tone refers to the degree of constriction or resistance in blood vessels [46]. Decreased temperature enhances vascular tone to preserve thermal homeostasis by retaining heat in the body's core, whereas increased temperature decreases vascular tone to shed excess heat in peripheral circulation. Overall, the changes in time delay observed in the post-exercise and cold pressor conditions demonstrate that this parameter is sensitive to vascular tone. This is particularly important because vascular resistance is a confounding factor in calculating blood pressure, cardiac output and fluid status [56] meaning that this technique could provide solutions for these medical applications.

This study only partially elucidates the implications of information embedded in the dual SPG-PPG signal. The cardiac pulse is progressively modified by mechanical properties of the underlying vasculature as it propagates down the arterial network. As light transmitted from a single coherent source interacts with the tissue, the pulsatile characteristics of the underlying cardiovascular system are ultimately contained in the SPG-PPG signal. We only present two ways of processing these signals, but there are many other methods that have not yet been explored. Examples include analyzing systolic upstroke time, dicrotic notch prominence, and other harmonic content ratios (in this work

we look only at the ratio of the third to the first harmonic). Further, almost every processing technique applied to PPG alone could be applied to this new framework. The SPG-PPG signal therefore constitutes a promising technology for continued research.

Overall, this study provides initial data to support the potential clinical significance of the SPG-PPG waveform. The SPG is distinct and possibly more robust than the PPG alone, as shown by the fact that the PPG waveform becomes weak and distorted with vascular constriction, while under these conditions the SPG signal retains its strength and pulsatility. This may be important because medical applications such as non-invasive cardiac output monitoring have failed due to issues with the PPG signal quality. We have also shown that the SPG and PPG signals provide different and complementary information, specifically flow speed pulsatility from the SPG and vascular expansion pulsatility from the PPG. The time-delay and pulse-shape characteristics of the SPG and PPG are evidence that they provide unique information, which is further supported by their differential response to contrasting physiological challenges. We conclude that wearable, affixed transmission LSI sensors can generate highly complementary SPG and PPG signals. They potentially provide a single, non-invasive platform for assessing vascular dynamics. Because of their relative simplicity and ease-of-use, ATSA devices may create new possibilities for non-invasive diagnostics and therapeutic guidance in circulatory diseases.

CHAPTER 4: REAL-TIME WIDE-FIELD MAPPING OF OXYGEN CONSUMPTION USING DUAL-WAVELENGTH COHERENT SPATIAL FREQUENCY DOMAIN IMAGING

4.1 Introduction

In this chapter, we present and validate a high-speed, dual-wavelength cSFDI system capable of imaging blood flow co-registered with [HbO_2] and [HHb] at 16 frames per second over large tissue regions and use this data to calculate $tMRO_2$. We validate chromophore measurements using a yeast-hemoglobin phantom in which hemoglobin is progressively desaturated using yeast. Additionally, we demonstrate sensitivity to chromophore concentration using a hemoglobin titration experiment in which portion of bovine red blood cells are added serially to a liquid phantom. We apply this technique to a five-minute arterial occlusion protocol and demonstrate the ability to measure changes in metabolism caused by ischemia and reperfusion in human subjects. Finally, we apply cSFDI to a rabbit model of cyanide poisoning and show sensitivity to mitochondrial uncoupling as well as the reversal of cyanide toxicity with hexachloroplatinate, a rapidly acting antidote.

4.2 Methods

4.2.1 Instrumentation

Figure 4.16 is a schematic of the cSFDI system. Two laser diodes were used as light sources: a 660 nm 150 mW Laser diode (HL6545MG, Opnext) and an 852 nm 150 mW laser diode (L852P150, ThorLabs). The current and temperature were stabilized using combined diode driver and TEC controllers (ITC4000, Thorlabs) to ensure stabilized power and speckle properties. Both diodes were mounted in thermoelectrically cooled diode mounts (LDM21, ThorLabs) and collimated using aspheric lenses. The beam path was combined

using a 785 nm hot mirror (FM01 ThorLabs) and two broadband dielectric mirrors for moving the beams into the correct position. An optical chopper (MC2000, ThorLabs) was used to multiplex between the two laser diodes. The laser beams were widened using a custom-built beam expander, transmitted through a ground glass diffuser, and condensed onto a sinusoidal-patterned slide (SF-4.0-80-TM-G, Applied Image). The pattern was then projected onto the sample using a 16 mm fixed focal length lens with VIS-NIR coating (#67-714, Edmund Optics). The sample is imaged using a high speed scientific CMOS camera (Hamamatsu Photonics, Orca Flash 4.0) with a wire grid polarizer (250 – 4000 nm WP25M-UB, Thorlabs Inc.) to remit specular reflections.

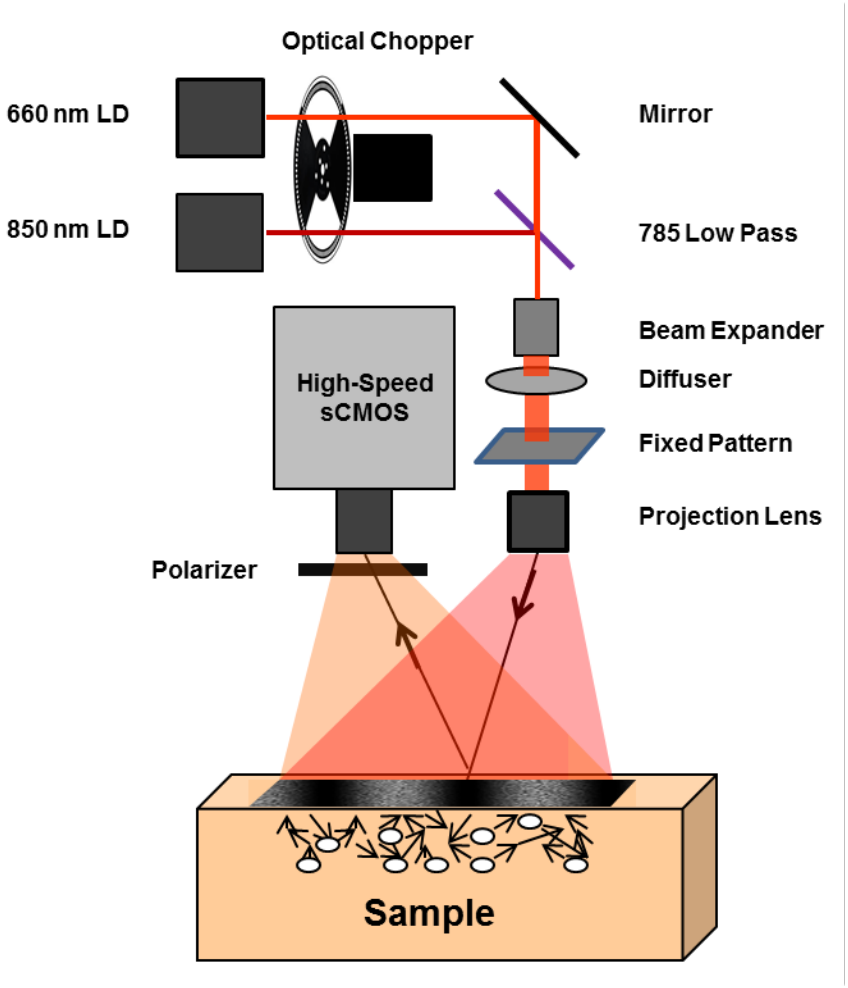

Figure 4.16 Schematic of Dual-Wavelength cSFDI. Two laser diodes (660 and 852 nm) are collimated and passed through an optical chopper blade. The beams are co-localized using a mirror and a 785 nm low pass such that both beams follow the same trajectory. The collimated lasers are but then passed through a beam expander and a diffuser before falling onto a fixed sinusoidal pattern. A projection lens is used to image the sinusoidal pattern onto the sample. The sample is imaged using a high speed sCMOS camera with a cross polarizer.

4.2.2 Data and Image Processing

Raw images were processed to create maps of SFI, [HbO_2], and [HHb] as outlined in Ghijsen et al. [57] and Cuccia et al. [17, 18]. Single raw images were used to simultaneously demodulate two spatial frequencies using algorithms originally described in Vervandier et

al. [33]. The data was calibrated using a phantom with known optical properties [38] to obtain the diffuse reflectance [17]. Optical properties at each wavelength were recovered pixel-by-pixel from the DC and AC reflectance using a Levenberg-Marquardt fit of experimental data to a light-transport model. Concentrations of oxyhemoglobin and deoxyhemoglobin were obtained using the absorption coefficient at both wavelengths (660 nm and 852 nm) and prior knowledge of the extinction coefficient spectra of HbO_2 and HHb [25].

The same data was used to simultaneously calculate the speckle flow index (SFI). A 7-pixel x 7-pixel sliding window filter was used to calculate the local standard deviation σ(I) and mean intensity <I>,which then used to compute the speckle contrast $K = \sigma / \langle I \rangle$ [57]. SFI is calculated from speckle contrast algebraically: $SFI = 1 / (2TK^2)$, in which T is the integration time [29].

4.2.3 Yeast-Hemoglobin-Intralipid Phantoms

Yeast-hemoglobin phantoms were used to validate dual-wavelength cSFDI in terms of recovering oxygen saturation. Yeast- Hemoglobin phantoms are liquid phantoms meant to imitate properties of real tissues with Bovine hemoglobin acting as the principle absorber and Intralipid acting as the principle scatterer [58, 59]. Figure 4.17a depicts the experimental setup for the yeast-hemoglobin phantom. A 15 cm x 15 cm Pyrex dish was used to hold the contents of the liquid phantom. A thermometer and Clark-electrode were used to monitor the temperature and partial pressure of oxygen, respectively. Bovine whole blood was centrifuged and washed with phosphate buffered saline to produce packed red cells. 50 mL of 20% Intralipid, 934 mL of 1% phosphate buffered saline, and 16 mL of packed bovine red blood cells were combined in the Pyrex dish. The contents were

then heated to 37° C using a hot plate. A magnetic stir bar was used to keep the contents well mixed.

After the contents were mixed together and brought to the proper temperature, the phantom was given time to equilibrate with the ambient oxygen tension. Next, baseline measurements were taken using both the Clark electrode and cSFDI. At this point, Yeast was dissolved in a small portion of warm water and was added to the solution. Measurements were taken continuously with cSFDI and the Clark electrode until the partial pressure of oxygen reached 0 mmHg.

4.2.4 Hemoglobin Titration Phantoms

This phantom was used demonstrate the capability of cSFDI to measure hemoglobin concentration compared with a validated system. The phantom was prepared similarly to the previous experiment. 934 mL of phosphate buffered saline was mixed together with 50 mL of 20% Intralipid (final concentration of 1%). During this procedure, 5 equal preparations of bovine packed red cells were added to the liquid phantom in series such that the concentration of hemoglobin increased in approximately equal amounts; it should be noted that the preparations were not exactly equal in terms of hemoglobin since evenly mixing red cells presents a technical challenge. The OX-Imager Rs (Modulated Imaging, Inc, Irvine, CA), a validated commercial SFDI system, was used for comparison. The hemoglobin titration phantom was measured before (Intralipid and PBS only) and in between serial addition of blood portions using both cSFDI and the OX-Imager Rs. No yeast was added to deoxygenate the hemoglobin and a Clark electrode was not used to monitor oxygen tension. After processing the data, baseline chromophore concentrations were subtracted

from cSFDI's chromophore concentrations to correct for the contribution of Intralipid to the absorption spectrum.

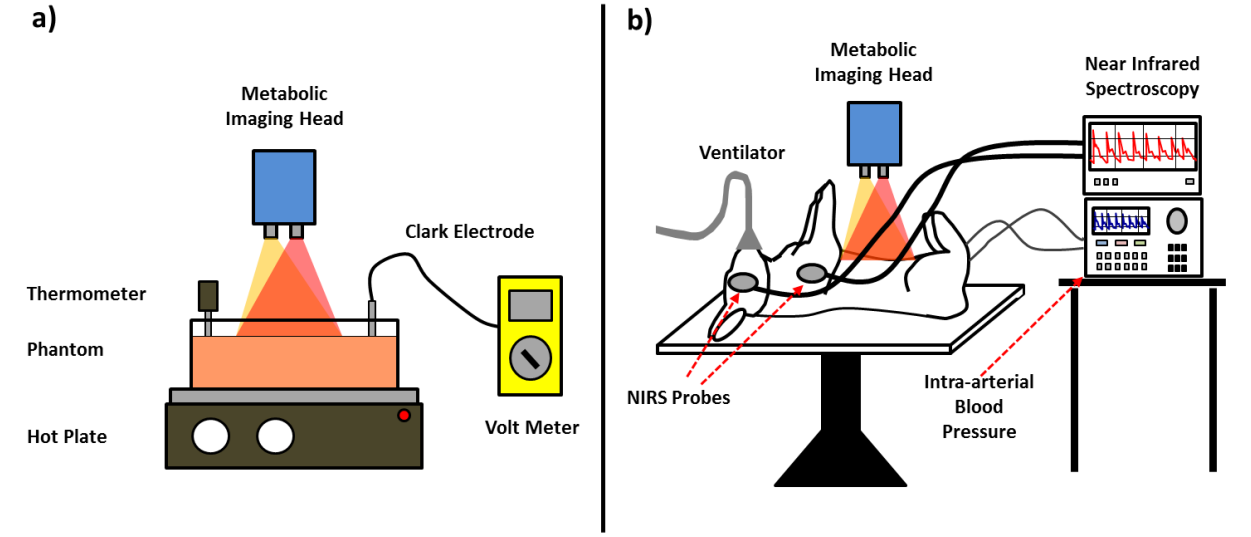

Figure 4.17 Cyanide-Rabbit-Model Experimental Setup. a) Yeast-Hemoglobin and Hemoglobin titration experiment. cSFDI is placed over a container holding the liquid phantom contents. A thermometer and Clark electrode are used to monitor the temperature and partial pressure of oxygen, respectively. A hot plate underneath the glass container keeps the phantom at 37 degrees and propels a magnetic stir bar within the phantom to keep the contents well-mixed. A volt meter is used to monitor the Clark electrode. b) Rabbit-cyanide experiment. The rabbit is placed supine on the operating table. CSFDI is placed over the lower abdomen. A ventilator is used sustain the anesthetized rabbit. Two NIRS probes are placed over brain and muscle regions to monitor saturation. Intra-vascular lines are inserted into the femoral artery and veins to monitor blood pressure and blood gases.

4.2.5 5-Minute Arterial Occlusion Experiment

A 5-minute arterial occlusion was performed on a healthy, 29-year-old male subject's left hand while being imaged with cSFDI. During this imaging procedure, the dorsal left hand was imaged while a full arterial occlusion was applied to the brachial artery using a pneumatic cuff inflated to 210 mmHg. The experiment consisted of 3 minutes of baseline (no occlusion), followed by 5 minutes of arterial occlusion, followed by 3 minutes of post-

release. 2D maps of [HbO_2], [HHb], and SFI were reconstructed for each time-point for a total of 10,560 time points (11 minutes x 60 seconds/minute x 16 frames/second). This data was then synthesized to produce $tMRO_2$ maps. Time-series data obtained from multiple regions of interest were used to analyze the metabolic physiology. The study was carried out under a UC Irvine IRB approved protocol and informed consent was obtained from the subject (HS #2011-8370).

4.2.6 Calculation of Metabolism

Indices of tissue metabolism were extracted from the 5-minute arterial occlusion data. This process was done in two parts: steady-state and occlusive. The steady-state refers to situations in which blood flows freely into and out of the tissue compartment of interest and [HbO_2] and [HHb] remain constant. In this situation, Fick's law can be invoked to relate the concentration of arterial oxygen ($[O_2]_a$) , blood flow (BF), and oxygen extraction fraction (OEF) with oxygen consumption [31]:

$$(1) \qquad tMRO_2 = (OEF)(BF)\,([O_2]_a)$$

OEF is the fraction of oxygen removed from arterial hemoglobin. In this work BF is blood flow normalized to a volume of tissue and ultimately contains units of inverse seconds (s^{-1}). Finally, $[O_2]_a$ is the molar concentration of *arterial* oxygen, having units of millimolar in this work. Furthermore, this model assumes arterial saturation is 100%.

It is possible to rearrange Fick's law and put it in terms of the tissue concentration of deoxyhemoglobin [HHb]:

$$(2) \qquad (OEF)([O_2]_a) = 4[HHb]$$

Additionally, normalized tissue blood flow (BF) can be put in terms of SFI:

$$(3) \qquad (BF) = (\alpha)(SFI)$$

In this equation, α is a constant that relates SFI with blood flow. This is necessary because even though SFI is linearly correlated with flow, it is not an absolute measurement of flow. Inserting (3) and (2) into (1):

$$(4) \qquad tMRO_2 = (\alpha)(SFI)(4[HHb])$$

Equation (4) is the calculation of the metabolic rate of oxygen consumption at steady-state written in terms of measurements that can be obtained using cSFDI.

During the occlusive state, blood flow is clamped off and no blood flows into or out of the tissue compartment; in this work, the forearm. In this situation, oxygen rate of metabolism can be calculated by measuring the rate at which [HbO_2] is converted to [HbR]. From Cheatle et al:

$$(5) \qquad tMRO_2 = 4\frac{d([HHb]_0)}{dt}$$

In this expression, MRO_2 is related to the first time-derivative of [HHb]. The factor of 4 is due to the fact that there are 4 oxygen molecules per hemoglobin tetramer.

Unlike equation (4), equation (5) provides a measurement of absolute metabolism since alpha is typically an unknown constant. However, alpha can be calculated if one has *a priori* knowledge of metabolism at a certain point in time. In the five-minute occlusion experiment, alpha can be calculated under the boundary condition that $tMRO_2$ at the beginning of the occlusion is continuous with metabolism prior to the onset of the occlusion. Intuitively, this assumption becomes less valid later in the occlusion period when oxygen becomes depleted, and $tMRO_2$ is reduced. Using the above boundary condition, (4) and (5) can be set equal to one another:

$$(6) \qquad (\alpha)(SFI_{bl})(4[HHb]_{bl}) = 4\frac{d([HHb]_0)}{dt}$$

In this expression, SFI_{bl} refers to average SFI at baseline, $[HHb]_{bl}$ refers to average deoxyhemoglobin concentration at baseline, and $[HHb]_0$ refers to the deoxyhemoglobin concentration at the beginning of the occlusion. Solving for alpha:

$$(7) \qquad \alpha = \frac{d([HHb]_0)}{dt} / \{(SFI_{bl})([HHb]_{bl})\}$$

This term can be reinserted into equation (4) to calculate the absolute $tMRO_2$ at baseline or following the release and was used to do so in this work.

For clarification, it is necessary to calculate α because it is not possible to directly determine $tMRO_2$ in the presence of blood flow. This is because SFI is not an *absolute* metric of perfusion. Instead, $tMRO_2$is calculated during arterial occlusion when flow is zero, and then α is obtained to scale metabolism in the non-occluded state. This is possible because SFI correlates linearly with flow.

4.2.7 Cyanide Rabbit Experiment

cSFDI was applied to a previously validated animal model in which a rabbit was infused with cyanide for a period of time and then given an antidote to reverse the poisoning [60, 61]. This was done to demonstrate cSFDI's ability to characterize metabolic changes due to cyanide exposure. Cyanide is a potent mitochondrial uncoupling agent that inhibits cytochrome c oxidase, decreasing oxygen consumption on the cellular level.

A New Zealand White Rabbit was anesthetized with Ketamine and Xylazine, intubated and placed on mechanical ventilation with 100% oxygen, and positioned supine as shown in figure 4.2. Invasive arterial and venous lines were placed in the left femoral artery and vein and used throughout the procedure to monitor blood gases. The cSFDI imaging head was positioned over the Rabbit's lower-right abdomen contralateral to the intravascular lines. The fur in the imaging area was removed using electric clippers and chemical hair-

remover. Before the procedure began, baseline measurements of cSFDI, arterial blood-gas, systemic pressure, heart-rate, and oxygen saturation were acquired. cSFDI was then used to monitor the animal through the entire experiment. Following baseline, the rabbit received a constant infusion of sodium cyanide at rate of 1 ml per minute for 55 minutes. The infusion had a concentration of 10 mg sodium cyanide per 50 ml of normal saline. After the infusion was completed the antidote (120 mg hexachloroplatinate in 120 μL dimethylsulfoxide and phosphate buffered saline) was administered. The animal was monitored for an additional hour following the antidote. At the end of the experiment, the rabbit was euthanized with pentobarbital. Data obtained with cSFDI was processed providing chromophores and SFI. The relative tissue metabolic rate of oxygen consumption ($rMRO_2$) was calculated using SFI and deoxyhemoglobin. This study was performed under Institutional Laboratory Animal Care and Use Committee protocol number 2000-2218.

4.3 Results

4.3.1 Yeast – Hemoglobin Experiment

Figure 4.3a shows the chromophore concentrations (left) and saturation (right) of the yeast-hemoglobin phantom obtained from a 1 cm x 1 cm region of interest (ROI) within the imaging field. The x-axis in both plots represents the partial pressure of oxygen determined using a Clark oxygen electrode. The plot of chromophores shows that total hemoglobin remains constant throughout the experiment. It also shows that at 0 mmHg partial oxygen pressure, [HbO_2] is roughly 0 milliMolar (mM). As partial pressure increases to 160 mmHg (ambient oxygen pressure), [HbO_2] increases to approximately the concentration of total hemoglobin, following a sigmoidal (s-shaped) curve characteristic of the hemoglobin desaturation. [HHb] follows the opposite trend. At 0 mmHg partial pressure of oxygen, the

mixture is completely composed of deoxyhemoglobin as evidenced by the fact that [HbT] and [HHb] are approximately equal. As the partial pressure of oxygen increases, [HHb] decreases along a sigmoidal curve until it settles at a concentration of about 0 mM. The error bars in the chromophore plot show the spatial variation contained within the region. Since the yeast-hemoglobin phantom is practically homogeneous, these intervals closely approximate the random system error with respect to chromophore concentration. With this in mind, the standard deviation in the random error taken from the [HbT] is 3%. The saturation plot on the right of figure 3a demonstrates that cSFDI is sensitive to the full range of saturation values i.e. that it can detect 0 to 100 % saturation. The curve also has the sigmoidal shape characteristic of hemoglobin.

4.3.2 Intralipid Hemoglobin Titration Experiment

Figure 4.3b shows the results from the hemoglobin titration experiment. The y-axis shows total hemoglobin concentration obtained with cSFDI and the x-axis shows results obtained using a validated commercial SFDI device (OxImager Rs, Modulated Imaging, Inc., Irvine, CA). Both axes are in arbitrary units due to the fact that the OxImager Rs uses proprietary software that does not specify units. These data demonstrate response linearity in terms of total hemoglobin recovery when compared with a standard commercial system. The accuracy of both technologies (SFDI and cSFDI) in terms of chromophore quantitation has been validated at length in previous work [17, 24]. This experiment is only intended to demonstrated linearity between the two instruments.

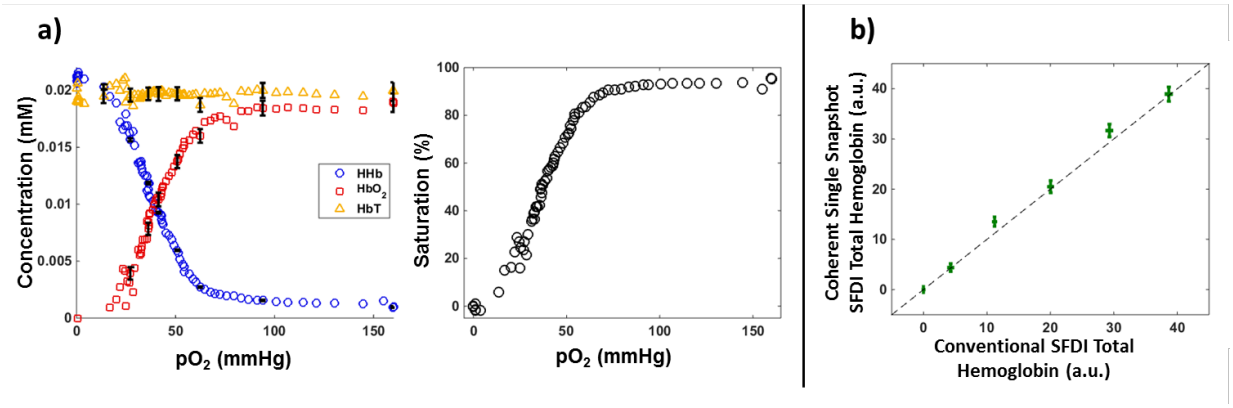

Figure 4.18 Yeast-Hemoglobin and Hemoglobin Titration Results. a) Yeast-Hemoglobin phantom results. The left panel shows blood saturation against partial pressure of oxygen. The right panel shows chromophore concentrations of deoxyhemoglobin, oxyhemoglobin, and total hemoglobin (D, O, and T, respectively). The error bars represent the standard deviation over the 80-pixel by 80-pixel ROI taken from a single frame. b) Hemoglobin titration results. The graph shows total hemoglobin concentration measured using dual-wavelength cSFDI vs. total hemoglobin concentration measured using standard commercial SFDI on the x-axis. These 2-dimensional error bars represent the standard deviation in each measurement over an 80-pixel x 80-pixel ROI taken from a single frame of raw data. The black dotted line is a reference line of equality.

4.3.3 5-minute arterial occlusion experiment

Figure 4.4 shows results from the arterial occlusion experiment. From left to right, the top 3 images show maps obtained during baseline (t = 0s) of SFI at 852 nm, [HHb], and [HbO_2]. SFI is in arbitrary units, and chromophore concentrations are in millimoles/L (mM). The green rectangle in the SFI image defines the 1 cm x 1 cm region of interest (ROI) from which the time-series data were obtained. The bottom left plot shows SFI at 852 nm in arbitrary units vs. time in seconds. The brown shaded region outlines the duration of the arterial occlusion; the period before the shaded region is the baseline and the period after is the post-release. The error bars overlaid on the SFI plot denote the standard deviation of the values contained within the ROI. The ROI is 80 pixels by 80 pixels taken from a single

frame of data i.e. multiple frames were not averaged. It should be noted that these margins are not only due to random instrument error, but also take into account spatial variations of tissue properties within the ROI. On average, the standard deviation taken from the ROI in total hemoglobin displayed in figure 4 is 4%, slightly higher than the instrument error of 3%. At the onset of the occlusion (t = 180 s), an instantaneous decrease in the SFI data is clearly observable. Likewise, upon release of the occlusion (t = 480 s) there is an instantaneous increase that overshoots baseline values. The average SFI at baseline is 36 arbitrary units (au) and the average of the first 30 seconds post-release is 74. During the occlusion the SFI drops to an average of 21 referred to as biological zero [62]. There are pulsatile spikes throughout the occlusion due to blood movement caused by muscle contractions from ischemic cramping. Subtracting biological zero from baseline and post-release averages, these data show that perfusion within this ROI is 340% higher during the first 30 seconds post-release than at baseline demonstrating sensitivity to post-occlusive reactive hyperemia.

The plot on the bottom-right of figure 4 depicts the time-series [HbT], [HbO_2], and [HHb] in yellow, red, and blue respectively. Once again, the brown shaded region outlines the arterial occlusion, with baseline and post-release coming before and after, respectively. The error bars overlaid on the chromophore plots denote the standard deviation of the ROI due to combined instrument and biological variation. [HbT] remains constant throughout the baseline and occlusion periods. [HbO_2] on the other hand decreases during the occlusion while [HHb] increases; both are the result of oxygen extraction. Following the release, there is a spike in [HbT] and [HbO_2] caused by reactive hyperemia. [HHb] decreases as it is washed out of the tissue compartment by fresh blood.

Within the large region corresponding to the black, dotted line in the [HHb] image, the mean [HbO_2] is 0.07 mM and the relative standard deviation (RSD) is 75%. In the same region, the average [HHb] and SFI were 0.025 mM and 59 au, respectively. The RSD values for [HHb] and SFI were 64% and 42%, respectively. In previous work, we demonstrated using phantom studies that cSDFI-derived optical properties (and material composition) vary by 3% over a large (15 cm x 15 cm) field of view. As a result, the more substantial variations seen in this work represent the heterogeneous nature of tissue where a predominantly capillary-irrigated region has properties that differ from a region with an underlying vein. Time-series data were extracted from the smaller 80-pixel by 80-pixel ROI in order to improve sensitivity to dynamic tissue-level changes. This is because spatial variation and differential temporal dynamics across the tissue lead to diminished signal quality when large ROIs are selected; the changes in one region are confounded by those in another.

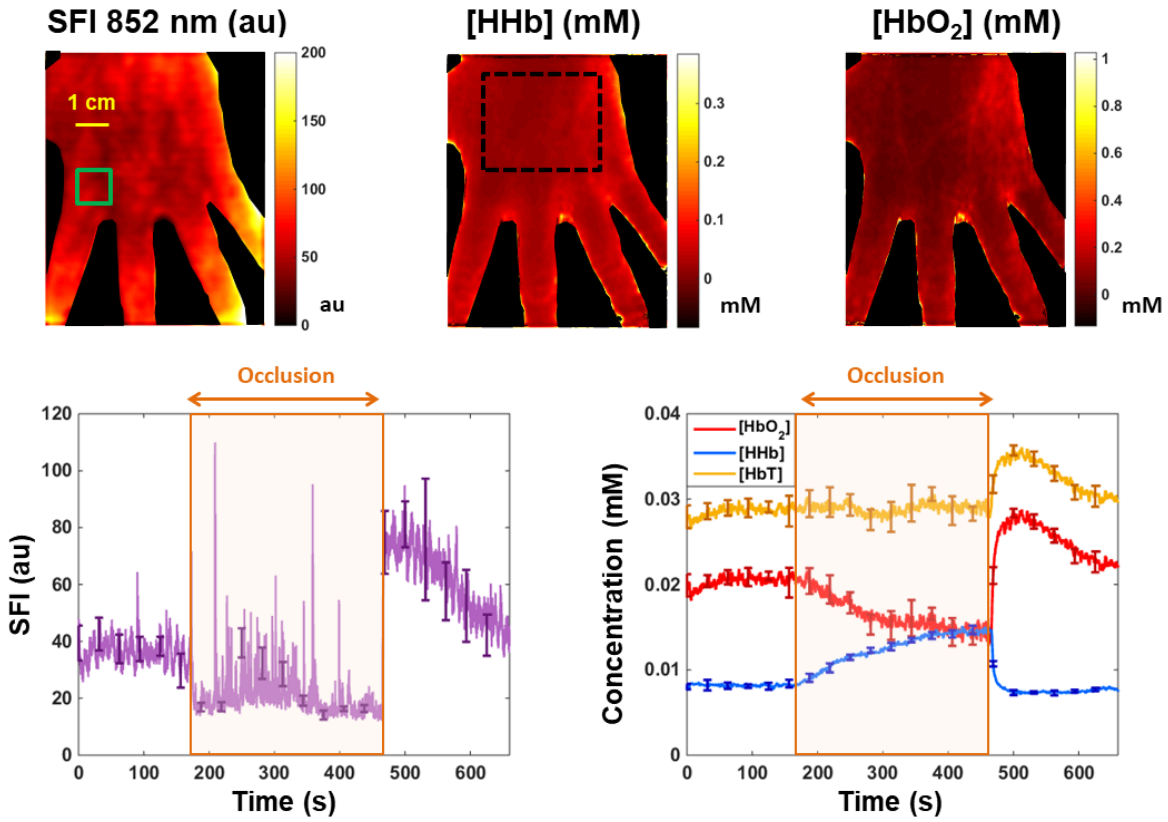

Figure 4.19 Arterial Occlusion Results. From left to right, the top row of images shows baseline (t = 0 s) maps of speckle flow index, deoxyhemoglobin, and oxyhemoglobin, respectively. Speckle flow is in arbitrary units while concentrations are millimoles per liter (mM). The bottom row shows time-series data taken from a 1cm x 1 cm ROI outlined in green in the SFI image. The left graph shows speckle flow index (SFI) vs. time while the right graph shows chromophore concentration vs. time. The left and right arrows in each graph show the beginning and end of the occlusion, respectively. The [HHb] image contains a black, dotted region used to calculate parameter means and variations.

4.3.4 Absolute and Relative Metabolism

Figure 4.5a demonstrates the synthesis of absolute and relative metabolism from SFI and [HHb]. The top plot presents time-series [HHb] obtained from a single region of interest (ROI). The black dotted line is a linear fit of the slope used to calculate $tMRO_2$ via equation (5). The red dotted line on either side of the slope depicts the average [HHb]

before and after the occlusion. Average baseline [HHb], denoted in the figure as $[HHb]_{bl}$, was inserted into equation (7). Average [HHb] post-release, denoted in the figure as [HHb], was inserted into equation (4). The bottom plot in figure 3a shows SFI at 852 nm. The black double-sided arrows represent baseline SFI (left) and post-release SFI (right). The biological zero value, defined as SFI during zero blood flow and depicted in the figure as the solid black line during the occlusion, is subtracted from the pre- and post-occlusion measurements in order to account for this offset. Baseline SFI (SFI_{bl}) is inserted into equation (7) in order to calculate α. Post-release SFI (denoted SFI) is inserted into equation (4). Absolute and relative metabolic rates of oxygen consumption were then determined by inserting the extracted parameters derived pictorially in figure 5a into equations 4, 5, and 7.

Figure 4.5b shows the relative and absolute metabolic rates from the pre-occlusion and post-release periods. The two intervals are separated by a break in the x-axis, depicted by the two parallel diagonal lines intersecting the top and bottom horizontal axes. The overall trend is depicted in the top-left plot of panel b, showing relative $tMRO_2$ in arbitrary units. At baseline (from approximately t = 50 – 150 seconds) there is no general trend. However, metabolism fluctuates sinusoidally with an amplitude approximately 50% of the DC-offset. During the post-release phase (t = 500 – 600 seconds), relative $tMRO_2$ starts out at approximately 4 au and gradually decreases back to baseline. Oscillatory fluctuations are simultaneously observed on top of this trend. The bottom left plot depicts absolute $tMRO_2$ in units of millimoles per liter per second. Relative $tMRO_2$ is calculated by dividing absolute $tMRO_2$ at a given time point during post-release by baseline $tMRO_2$.

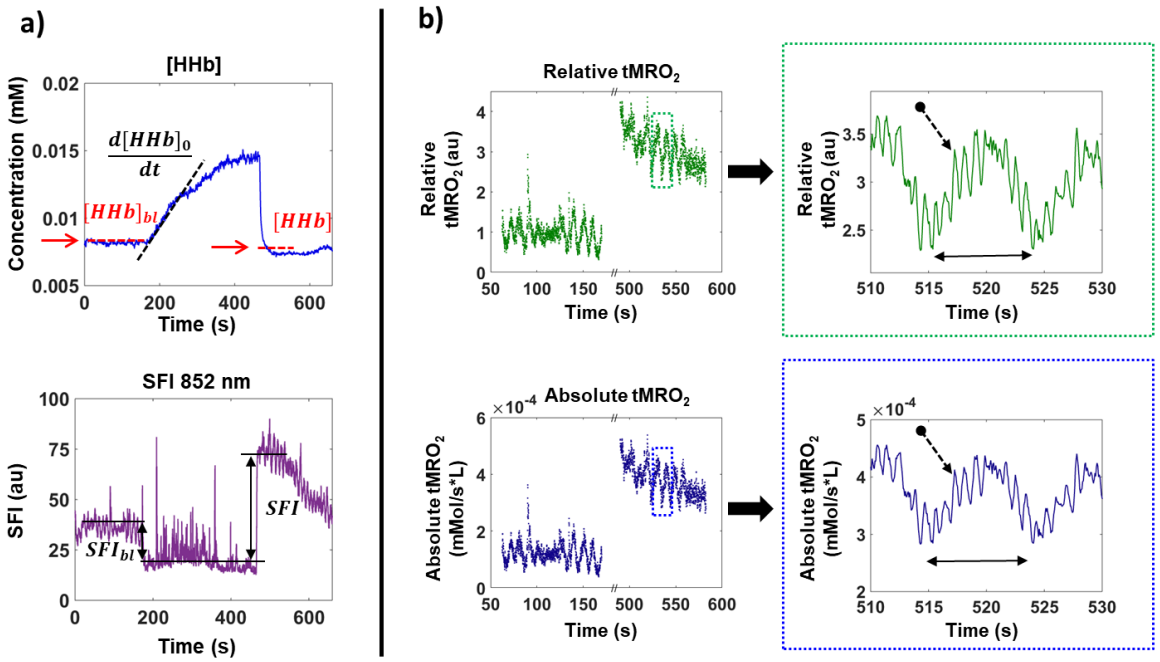

Figure 4.20 Metabolic Calculation Schematic. Panel a) contains the cSFDI parameters used to calculate absolute and relative tissue metabolic rates of oxygen consumption ($tMRO_2$). The top plot in panel a) shows deoxyhemoglobin concentration and the bottom plot shows speckle flow index (SFI) at 852 nm throughout the arterial occlusion protocol. Panel b) contains relative and absolute $tMRO_2$. The two plots in green along the top contain relative metabolism and the two plots along the bottom contain absolute metabolism. The plots on the left contain the baseline and post-occlusion time-series data and are separated by a break in the x-axis. The plots on the right of panel b contain an expanded view of a 20 second period (510-530 seconds) obtained from the dotted rectangles in the plots on the left.

The top-right plot shows a magnified region of the relative $tMRO_2$ data extracted from the green, dotted rectangle in the top-left plot. This expanded view clearly shows Mayer waves (double-sided arrow) with a period of about 10 seconds. Mayer waves are slow oscillations due to sympathetic regulation of vascular tone. Within this 0.1 Hz oscillation, the heartbeat is also clearly visible (arrow with dotted line) with a period of slightly less than one second. The bottom-right plot shows the absolute metabolism corresponding to

the same time period. Again, the double-sided arrow represents the period of the Mayer waves and the dotted arrow points to the heartbeat. Overall, these signals demonstrate cSFDI sensitivity to $tMRO_2$ dynamics throughout the post-release phase.

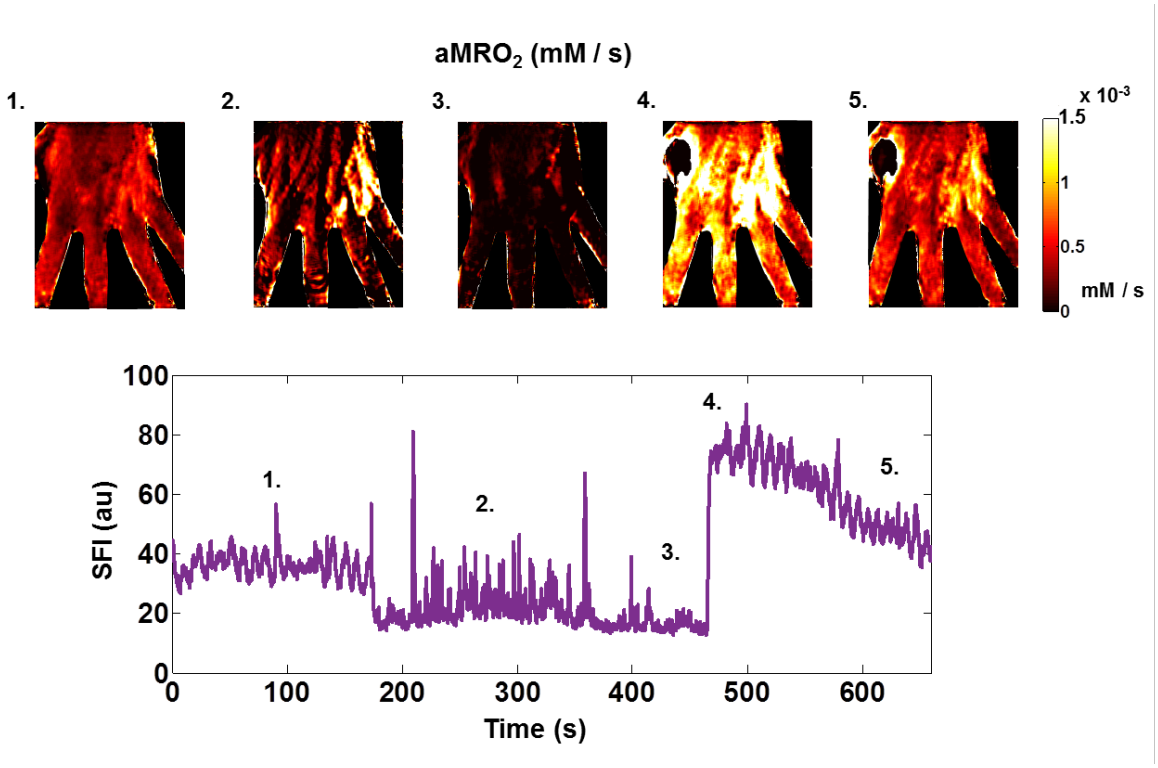

Figure 4.21: Tissue Metabolic Rate of Oxygen Consumption ($tMRO_2$) Property Maps. The images along the top are maps of $tMRO_2$ in mM/s (millimoles per liter per second). The bottom plot shows the speckle flow index (SFI) obtained at 852 nm from a ROI. The numbers at the top left of each $tMRO_2$ image correspond to the times in the SFI plot. Image 1 was calculated at baseline, images 2 and 3 were calculated at different times during the occlusion, and images 4 and 5 were calculated at different times following the release.

The images along the top of figure 4.6 show $tMRO_2$ maps in millimoles per liter per second at different times throughout the arterial occlusion protocol. The plot beneath the images shows the same SFI time-series data presented in figure 4.6 and is provided as a reference for the $tMRO_2$ image sequence. The numbers at the top left of each image correspond to the numbers in the SFI plot. Image 1 is taken from the entire baseline duration from 0 – 180 s

(see methods section for details). Images 2 and 3 were calculated from the middle to end of the occlusion and correspond to 260 s and 480 s, respectively. Both images 2 and 3 required a linear fit to [HHb] as described in the methods section. Images 4 and 5 were derived from the post-release phase and correspond to 490 s and 600 s, respectively. The $tMRO_2$ images demonstrate a progressive reduction in tissue metabolic rate during the occlusion. These data also demonstrate a substantial increase in $tMRO_2$ associated with the release of the occlusion that gradually decreases with repayment of the oxygen debt.

Table 4.1 presents the average metabolic parameters calculated for 3 subjects aged 29 – 46 who took part in the arterial occlusion protocol. Subject 1 underwent a 5-minute occlusion while subjects 2 and 3 underwent 3-minute occlusions. The baseline, intra-occlusion and post-occlusion metabolism are provided in units of millimoles of oxygen per liter per second (mM/s) and the relative metabolism is given in arbitrary units. The table provides the mean and standard deviation of each parameter calculated over 100 separate 10-pixel x 10-pixel ROIs (6 mm by 6 mm). The baseline metabolism is calculated from the first 30 seconds of the arterial occlusion, while the intra-occlusion metabolism is calculated from the final 30 seconds of the arterial occlusion. For the rationale behind using the first 30 seconds for baseline, see the methods section 2.6. The relative metabolism is the average ratio of the post-occlusion metabolism to the baseline metabolism. Because this ratio is calculated at each ROI and *then* averaged, it is not exactly equal to the ratio of the baseline to post-occlusion values provided in the table 4.

Table 4.1 Average Metabolic Calculations. Each entry contains the mean and standard error calculated from 100 separate 10-pixel x 10-pixel regions (6 mm x 6 mm).

	Subject 1	Subject 2	Subject 3	Units
Baseline Metabolism	$(3.5 \pm 0.09) \times 10^{-4}$	$(2.7 \pm 0.07) \times 10^{-4}$	$(2.9 \pm .1) \times 10^{-4}$	mM / s
Intra-Occlusion Metabolism	$(9.8 \pm 1.4) \times 10^{-5}$	$(1.9 \pm 0.08) \times 10^{-4}$	$(1.0 \pm .09) \times 10^{-4}$	mM / s
Post-Occlusion Metabolism	$(10 \pm 1.6) \times 10^{-4}$	$(7.8 \pm 1.8) \times 10^{-4}$	$(6.7 \pm 0.2) \times 10^{-4}$	mM / s
Relative Metabolism	4.6 ± 0.9	3.8 ± 0.8	3.1 ± 0.05	a.u.

4.3.5 Cyanide Rabbit Experiment

Figure 4.7 presents metabolic imaging data acquired from the rabbit model of cyanide poisoning. The time-series data in each plot are derived from a 1 cm x 1 cm region of interest (ROI) within the lower right abdomen. From left to right, the top row presents plots of percent change in deoxyhemoglobin (%ΔHHb), percent change in oxyhemoglobin (%ΔHbO_2), and percent change in total hemoglobin (%ΔTHb). From left to right, the bottom row shows percent change in tissue saturation (%ΔStO_2), percent change in speckle flow index (ΔSFI), and percent change in relative metabolism (%$\Delta rMRO_2$). In each graph, the x-axis represents time in minutes. The brown shaded box outlines the duration of the cyanide infusion. The antidote is administered immediately after the cyanide infusion ends, visually depicted as the right edge of the brown, shaded box.

Deoxyhemoglobin, pictured in the top-middle panel, decreases by 35% from baseline (t = 0 minutes) to the end of the cyanide infusion (t = 60 minutes). After the cyanide infusion is stopped and the antidote is administered at t = 60 minutes, deoxyhemoglobin eventually increases by 45% by the end of the experiment at t = 120 minutes. Oxyhemoglobin, pictured in the top-left panel, decreases by 5 % throughout the infusion of cyanide. Following the end of the cyanide infusion and the antidote bolus, the oxyhemoglobin begins to fluctuate erratically before returning to baseline at the end of the experiment (t = 120 minutes). Total hemoglobin, pictured in the top-right panel, decreases by 8% during the cyanide infusion (t = 60 minutes), and then eventually returns to baseline following the antidote (t = 120 minutes). Tissue saturation, pictured in the bottom-left panel, increases by 3% from the beginning (t = 0 minutes) to the end (t = 60 minutes) of the cyanide infusion. It then decreases by 4 percent from the end of the infusion and the administration of the antidote (t = 60 minutes) to the end of the experiment (t = 120 minutes). SFI obtained from the 660 nm laser diode, pictured in the bottom center plot of figure 7, remains relatively constant throughout the infusion, and then decrease by 25% from the end of the infusion (t = 60 minutes) to the end of the experiment (t = 120 minutes). In this experiment, 660 nm was used for SFI because of better signal quality (vs. 852 nm), possibly due to rabbit skin having different characteristics than human skin. Relative metabolism, pictured in the bottom-right panel, decreases by 25 % from baseline (t = 0 minutes) to the end of the infusion (t = 60 minutes). It then increases by approximately 15 percent from the end of the infusion / administration of the antidote (t = 60 minutes) to the end of the experiment (t = 120 minutes).

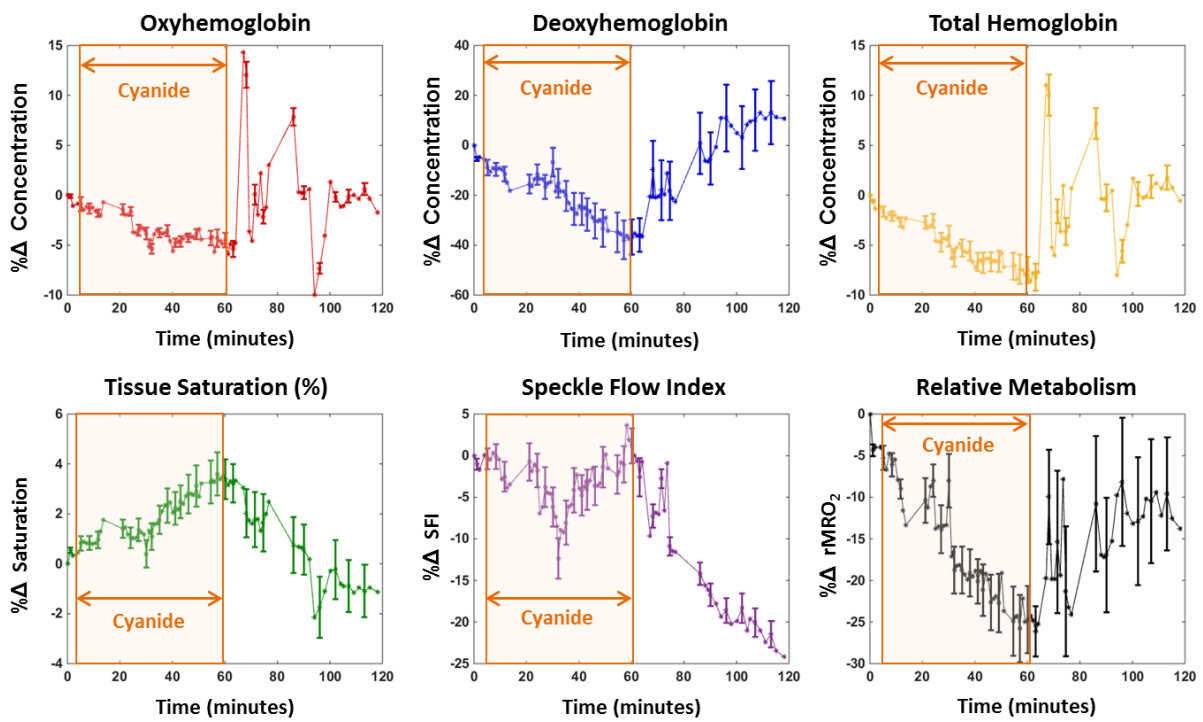

Figure 4.22: Rabbit Cyanide cSFDI Experimental Results. Along the top from left to right, the plots contain the percent change from baseline in tissue concentrations of deoxyhemoglobin, oxyhemoglobin and total hemoglobin, respectively. Along the bottom from left to right, the plots contain percent change in tissue saturation, speckle flow index (SFI), and relative tissue metabolic rate of oxygen consumption ($rMRO_2$).

4.4 Discussion

The development of quantitative, non-contact, label-free methods for real-time imaging of tissue metabolism over a wide, scalable field-of-view would have broad impact in medical imaging and image-guided therapy. In this work we introduce several technical innovations to achieve this goal based on the sinusoidal projection of two long-coherence-length, near infrared (NIR) laser diodes at a fixed spatial frequency pattern ($f = 0.2\ mm^{-1}$). Using a single snapshot Fourier demodulation technique and model-based analysis of light transport in the spatial frequency domain, we simultaneously acquire the speckle flow

index (SFI) while generating tissue oxy- and deoxyhemoglobin concentration maps. By combining the coregistered SFI and tissue hemoglobin parameters we demonstrate that $tMRO_2$ can be acquired at sufficiently high speed (16 frames/s in this work) to reveal spatial and temporal dynamics in tissue metabolism that are otherwise difficult or impossible to measure.

Dual-wavelength single snapshot cSFDI, utilizes only one projection frequency per wavelength allowing for fast measurements and simplified instrumentation. Since only a single detector is used in acquisition, there is intrinsic coregistration of all parameters which simplifies the synthesis of tissue chromophore and SFI data into $tMRO_2$. An important feature of this technique is that spatial modulation allows cSFDI to decouple tissue optical properties, i.e. absorption (μ_a) from reduced scattering (μ_s') parameters, in order to produce more accurate quantitative tissue measurements compared to conventional unstructured illumination [17]. Tissue [HbO_2] and [HHb] are then calculated directly from dual-wavelength μ_a values. Reduced scattering, although not explored in this work, is also an important parameter with relevance to burn wound classification and tissue structural orientation [34, 63].

Yeast-hemoglobin tissue phantom experiments validate cSFDI performance over the full range of hemoglobin saturation values, reproduce the correct sigmoidal desaturation curve, and linearly quantify [HHb] and [HbO_2] compared to a conventional commercial SFDI device. We note that the conventional SFDI method used for comparison employed 3 optical wavelengths, 5 spatial frequencies at each optical wavelength, and 3 spatial phases for each frequency. As a result, a total of 45 raw images (3 x 5 x 3) were used for each measurement. By comparison, dual-wavelength single snapshot cSFDI used only 2 optical

wavelengths and 2 spatial frequencies (f = 0 and 0.2 mm^{-1}). Importantly, these 2 spatial frequencies are embedded within a single image and do not require 3 spatial phases, yielding a total of just 2 raw images per measurement, thus enabling a much higher sampling rate. However, as a consequence dual-wavelength cSFDI is unable to account for additional chromophores, which is why baseline optical properties were subtracted in the yeat-hemoglobin phantom study. This is due to the fact that Intralipid has a nonzero extinction coefficient. Together, the yeast-hemoglobin and hemoglobin titration experiments indicate that cSFDI has the potential to accurately measure $tMRO_2$ insofar as chromophore recovery is accurate. In previous studies we have shown that the speckle flow index (SFI) obtained using cSFDI is linear and robust with respect to volumetric flow [57], hence we did not perform additional validation of flow properties in this work.

In vivo human arterial occlusion studies demonstrate that cSFDI can measure dynamic changes relevant to human physiology. The chromophore time-series data in figure 4 show sensitivity to oxygen extraction during the occlusion with increasing [HHb] and decreasing [HbO_2]. However, total hemoglobin [HbT] remains constant which suggests that, as expected, blood does not enter or leave the compartment during an arterial-venous occlusion. The SFI tracings also demonstrate the ability to measure physiologic changes. In figure 4, SFI drops immediately to a residual level (biological zero) during the occlusion and it increases immediately after the occlusion to a level substantially higher than baseline. This accurately reflects what is known to happen physiologically. At the onset of the occlusion, blood flow to the subject's arm is instantaneously clamped off using a pneumatic cuff. When the occlusion is released, blood flow immediately spikes to a higher level than at baseline. This is further evidence that cSFDI can detect post-occlusive reactive

hyperemia – the increase in blood flow following occlusion caused by accumulation of metabolic byproducts. [HbT] and [HbO_2] also show a spike following the occlusion due to this same effect.

Integrating this information into metabolism tells a more complete story. The $tMRO_2$ data show clear evidence of decreased metabolism due to ischemia during the occlusion as well as increased $tMRO_2$ associated with oxygen debt repayment brought on by the release. Being able to detect this information is important for a number of reasons. In PAD patients whose limbs are subject to chronic ischemia, tissue has adaptively reduced oxygen consumption meaning that an ischemic challenge would not be expected to affect the tissue as severely. In such situations the oxygen debt accrued by the arterial challenge would be measurably less than in a healthy subject. In this clinical setting, cSFDI could provide a valuable means for tissue metabolic characterization for therapeutic monitoring and disease stratification. It is also important to emphasize that the $tMRO_2$ data presented in figures 5 and 6 indicate that metabolism is not static. Figure 5 in particular shows there is a substantial reduction in $tMRO_2$ during the post-release period in addition to large variations brought on by sympathetic fluctuations in blood pressure (Mayer waves) and the heartbeat. This reinforces the significance of real-time measurements for accurately characterizing dynamic metabolism. If the acquisition time for a single measurement were not sufficiently short, these trends would be averaged out.

Previous measurements of skin oxygen consumption using oxygen electrodes recorded an average dermal respiration rate of 1470 mL O_2 min^{-1} m^{-3} [64]. In comparison cSFDI yields average baseline skin oxygen consumption rates of $3.0x10^{-4}$ mM/s (Table 1) which can be converted to 514 mL O_2 min^{-1} m^{-3} at skin temperature of 34°C. There are a number

of potential reasons why these measurements differ. cSFDI is based on noncontact optical imaging of blood flow and hemoglobin whereas Evans and Naylor [64] utilized oxygen tension sensitive needle-electrodes inserted into the dermis. Needle electrodes probe a finite dermal region close to the electrode tip whereas cSFDI interrogates a relatively large tissue volume with contributions from epidermis, dermis, subcutaneous fat and connective tissue. The presence of low oxygen consumption rate tissues, such as subcutaneous fat and connective tissue within the cSFDI measurement compartment, likely account for this discrepancy. Importantly, the 3.1- to 4.6-fold increase in cSFDI measured metabolism following 3- and 5-minute occlusions, respectively, is proportional to the increasing duration of oxygen debt. This is also similar to what has been seen in studies using invasive oxygen electrodes [65] and further supports the sensitivity and realistic performance estimates of cSFDI metabolic measurements.

Finally, experiments using a rabbit model of cyanide poisoning show that cSFDI is capable of detecting mitochondrial uncoupling brought on by inhibition of Cytochrome C Oxidase. During the 60-minute cyanide infusion, cSFDI detected an increase in saturation of 3% and a decrease in relative metabolism of about 40%. The trend in the saturation obtained with cSFDI agrees with previous work involving Diffuse Optical Spectroscopy (DOS) which showed a 10% increase in tissue saturation under similar experimental conditions [60]. The difference in saturation changes may be attributable to the difference in measurement volumes in that cSFDI measures superficial tissue whereas DOS measures the underlying muscle.

The experiment also demonstrates the advantage of extracting $tMRO_2$ vs. tissue hemoglobin oxygen saturation (StO_2) alone. If StO_2 were the only output, the cyanide

infusion response could be interpreted incorrectly as increased tissue perfusion. This is due to the fact that, for a given tissue, increasing StO_2 levels normally indicate reduced oxygen extraction and increased tissue blood flow. However, the SFI data alone clearly show that flow did not increase during the cyanide infusion. As a result, cSFDI measurements provide a more complete picture of the underlying physiology and reveal difficult-to-measure uncoupling of blood flow and metabolism. Because metabolic uncoupling can occur in a variety of tissue pathologic states, methods for rapidly characterizing and imaging the magnitude and spatial extent of this phenomenon are expected to have utility in clinical and translational medicine.

CHAPTER 5: CONCLUSIONS AND FUTURE DIRECTIONS

The body of this work focuses on high-speed coherent light assessment using two modalities: Coherent Spatial Frequency Domain Imaging (cSFDI) and Affixed Transmission Speckle Analysis (ATSA). The goal of this work is to develop strategies for cardiovascular health assessment using noninvasive coherent light techniques. To this end, we have described and demonstrated novel instrument builds and processing methods capable of measuring physiological tissue characteristics. We achieve this by applying coherent light techniques, which have the ability to measure both blood flow and blood volume (whether it be pulsatile vascular changes as seen with ATSA or oxy- and deoxyhemoglobin concentration as measured with cSFDI). What's more, we make improvements in instrumentation producing high-speed data acquisition that can measure dynamic tissue fluctuations.

In Chapter 2 of this dissertation we presented and validated high-speed single snapshot cSFDI. We have showed the ability to accurately recover optical properties (μ_a and μ_s') using homogeneous phantoms. We have also demonstrated the recovered SFI values are linear with respect to absolute volumetric flow. Applying this technique to an arterial occlusion protocol we demonstrated sensitivity to the phenomenon of reactive hyperemia. In addition, we have shown it is possible to extract the cardiac waveform from the SFI channel. This technique was developed with the dual purpose of measuring metabolism and to probing hemodynamics pulsatile fluctuations.

In Chapter 3 we presented novel processing algorithms for the SPG-PPG signal and introduced time-delay and harmonic content. We demonstrated a correlation between these parameters and age; time-delay is positively correlated with subject age, and harmonic

content is negatively correlated with subject age. This indicates that these methods have potential for monitoring arterial stiffness, an important property in cardiovascular illness. We also demonstrated changes in time-delay that are related to vascular tone. This indicates that time-delay may play an important role in measuring vascular resistance, and important factor in noninvasively determining cardiac output.

In Chapter 4 we presented High Speed Dual-Wavelength cSFDI and its application to $tMRO_2$ imaging. We demonstrate the ability to obtain μ_a, μ_s', and SFI at 2 judiciously chosen wavelengths (660 and 852 nm) and thus able to recover oxyhemoglobin, deoxyhemoglobin in addition to relative blood flow. We validated chromophore accuracy using a series of liquid phantom experiments. In addition, we introduced a framework for measuring metabolism and applied this frame work to arterial occlusion experiments in which we were able to demonstrate sensitivity to increased metabolism caused by the accrued oxygen debt. Additionally, we deploy this system in a cyanide rabbit model and demonstrate the ability to measure decreased metabolism caused by decoupling of oxidative phosphorylation.

Future work will apply $tMRO_2$ clinical imaging to early diagnostic and therapeutic monitoring of Peripheral Arterial Disease (PAD). In PAD, progressive atherosclerosis over time leads to decreased perfusion ultimately culminating in decreased tissue function. Current treatment paradigms hinge on endovascular interventions which avulse material from within the lumen of peripheral arteries in order to restore perfusion. This is done by feeding a small wire through the arteries and scarping the sides clean with a special tool attached to the leading end. Depending on the extent of disease, an expanding metal mesh known as a stent may be placed within the vessel to maintain patency. The physician performing these interventions determines procedural success by injecting contrast and

imaging with x-rays to demonstrate vessel integrity. If perfusion is restored based on fluoroscopic assessment, the intervention is deemed a "technical success." Although these interventions effectively improve outcomes over large populations, not all patients experience diminished symptoms. This is confounded by the fact that technical success is not predictive of outcome; fluoroscopic evidence of restored arterial perfusion is not always correlated with recovering tissue. It is hypothesized that underlying small vessel disease causes compromised microvascular function. In these instances, decreased capillary flow results in significantly reduced oxygen consumption as an adaptive mechanism for chronic ischemia. An imaging technique that quantitatively assesses microvascular function through metabolic rate quantitation could provide an effective therapeutic monitoring strategy. In future work, we plan to measure individuals with PAD before and after undergoing intravascular procedures such as angioplasty and stenting. We hypothesize that increases in $tMRO_2$ following the intervention will be correlated with improved tissue functional status and positive clinical outcomes. Overall, this could provide a point-of-care tool that is able to guide therapy and optimize response to therapy.

REFERENCES

1. Sette, G., et al., *Local brain haemodynamics and oxygen metabolism in cerebrovascular disease.* Brain, 1989. **112**(4): p. 931-951.

2. Bishop, S.P. and R.A. Altschuld, *Increased glycolytic metabolism in cardiac hypertrophy and congestive failure.* American Journal of Physiology--Legacy Content, 2016. **218**(1): p. 153-159.

3. Hsu, P.P. and D.M. Sabatini, *Cancer cell metabolism: Warburg and beyond.* Cell, 2008. **134**(5): p. 703-707.

4. Boroughs, L.K. and R.J. DeBerardinis, *Metabolic pathways promoting cancer cell survival and growth.* Nature cell biology, 2015. **17**(4): p. 351-359.

5. Hirsch, A.T., et al., *ACC/AHA 2005 Practice Guidelines for the management of patients with peripheral arterial disease (lower extremity, renal, mesenteric, and abdominal aortic): a collaborative report from the American Association for Vascular Surgery/Society for Vascular Surgery, Society for Cardiovascular Angiography and Interventions, Society for Vascular Medicine and Biology, Society of Interventional Radiology, and the ACC/AHA Task Force on Practice Guidelines (Writing Committee to Develop Guidelines for the Management of Patients With Peripheral Arterial Disease): endorsed by the American Association of Cardiovascular and Pulmonary Rehabilitation; National Heart, Lung, and Blood Institute; Society for Vascular Nursing; TransAtlantic Inter-Society Consensus; and Vascular Disease Foundation.* Circulation, 2006. **113**(11): p. e463-654.

6. Ishii, K., et al., *Decreased medial temporal oxygen metabolism in Alzheimer's disease shown by PET.* The Journal of Nuclear Medicine, 1996. **37**(7): p. 1159.

7. Tandara, A.A. and T.A. Mustoe, *Oxygen in wound healing—more than a nutrient.* World journal of surgery, 2004. **28**(3): p. 294-300.

8. Strauer, B.-E., *Myocardial oxygen consumption in chronic heart disease: role of wall stress, hypertrophy and coronary reserve.* The American journal of cardiology, 1979. **44**(4): p. 730-740.

9. Young, H., et al., *Measurement of clinical and subclinical tumour response using [18 F]-fluorodeoxyglucose and positron emission tomography: review and 1999 EORTC recommendations.* European journal of cancer, 1999. **35**(13): p. 1773-1782.

10. Ogawa, S., et al., *Brain magnetic resonance imaging with contrast dependent on blood oxygenation.* Proceedings of the National Academy of Sciences, 1990. **87**(24): p. 9868-9872.

11. Leproux, A., et al., *Assessing tumor contrast in radiographically dense breast tissue using Diffuse Optical Spectroscopic Imaging (DOSI).* Breast Cancer Research, 2013. **15**(5): p. R89.

12. Cerussi, A., et al., *Predicting response to breast cancer neoadjuvant chemotherapy using diffuse optical spectroscopy.* Proceedings of the National Academy of Sciences, 2007. **104**(10): p. 4014-4019.

13. Tromberg, B.J., et al., *Non–invasive measurements of breast tissue optical properties using frequency–domain photon migration.* Philosophical Transactions of the Royal Society B: Biological Sciences, 1997. **352**(1354): p. 661-668.

14. Durduran, T. and A.G. Yodh, *Diffuse correlation spectroscopy for non-invasive, micro-vascular cerebral blood flow measurement.* Neuroimage, 2014. **85**: p. 51-63.

15. Yu, G., et al., *Validation of diffuse correlation spectroscopy for muscle blood flow with concurrent arterial spin labeled perfusion MRI.* Optics express, 2007. **15**(3): p. 1064-1075.

16. Yazdi, H.S., et al., *Mapping breast cancer blood flow index, composition, and metabolism in a human subject using combined diffuse optical spectroscopic imaging and diffuse correlation spectroscopy.* Journal of Biomedical Optics, 2017. **22**(4): p. 045003-045003.

17. Cuccia, D.J., et al., *Quantitation and mapping of tissue optical properties using modulated imaging.* Journal of biomedical optics, 2009. **14**(2): p. 024012-024012-13.

18. Cuccia, D.J., et al., *Modulated imaging: quantitative analysis and tomography of turbid media in the spatial-frequency domain.* Opt. Lett, 2005. **30**(11): p. 1354-1356.

19. Choi, B., N.M. Kang, and J.S. Nelson, *Laser speckle imaging for monitoring blood flow dynamics in the in vivo rodent dorsal skin fold model.* Microvascular research, 2004. **68**(2): p. 143-146.

20. Briers, J.D., *Laser Doppler and time-varying speckle: a reconciliation.* JOSA A, 1996. **13**(2): p. 345-350.

21. Rice, T.B., et al., *Quantitative determination of dynamical properties using coherent spatial frequency domain imaging.* JOSA A, 2011. **28**(10): p. 2108-2114.

22. Rice, T.B., et al., *Determination of the effect of source intensity profile on speckle contrast using coherent spatial frequency domain imaging.* Biomedical optics express, 2012. **3**(6): p. 1340-1349.

23. Gioux, S., et al., *Three-dimensional surface profile intensity correction for spatially modulated imaging.* Journal of biomedical optics, 2009. **14**(3): p. 034045-034045-11.

24. Mazhar, A., et al., *Laser speckle imaging in the spatial frequency domain.* Biomedical optics express, 2011. **2**(6): p. 1553-1563.

25. Mazhar, A., et al., *Wavelength optimization for rapid chromophore mapping using spatial frequency domain imaging.* Journal of biomedical optics, 2010. **15**(6): p. 061716-061716-9.

26. Duncan, D.D. and S.J. Kirkpatrick, *Can laser speckle flowmetry be made a quantitative tool?* JOSA A, 2008. **25**(8): p. 2088-2094.

27. Kirkpatrick, S.J., D.D. Duncan, and E.M. Wells-Gray, *Detrimental effects of speckle-pixel size matching in laser speckle contrast imaging.* Optics letters, 2008. **33**(24): p. 2886-2888.

28. Dunn, A.K., et al., *Dynamic imaging of cerebral blood flow using laser speckle.* Journal of Cerebral Blood Flow & Metabolism, 2001. **21**(3): p. 195-201.

29. Ramirez-San-Juan, J.C., et al., *Impact of velocity distribution assumption on simplified laser speckle imaging equation.* Optics express, 2008. **16**(5): p. 3197-3203.

30. Boas, D.A. and A.K. Dunn, *Laser speckle contrast imaging in biomedical optics.* Journal of biomedical optics, 2010. **15**(1): p. 011109-011109-12.

31. Blockley, N.P., et al., *A review of calibrated blood oxygenation level-dependent (BOLD) methods for the measurement of task-induced changes in brain oxygen metabolism.* NMR in Biomedicine, 2013. **26**(8): p. 987-1003.

32. Dunn, A.K., et al., *Spatial extent of oxygen metabolism and hemodynamic changes during functional activation of the rat somatosensory cortex.* Neuroimage, 2005. **27**(2): p. 279-290.

33. Vervandier, J. and S. Gioux, *Single snapshot imaging of optical properties.* Biomedical optics express, 2013. **4**(12): p. 2938-2944.

34. Nadeau, K.P., A.J. Durkin, and B.J. Tromberg, *Advanced demodulation technique for the extraction of tissue optical properties and structural orientation contrast in the spatial frequency domain.* Journal of biomedical optics, 2014. **19**(5): p. 056013-056013.

35. Corlu, A., et al., *Uniqueness and wavelength optimization in continuous-wave multispectral diffuse optical tomography.* Optics letters, 2003. **28**(23): p. 2339-2341.

36. Konecky, S.D., et al., *Imaging scattering orientation with spatial frequency domain imaging.* Journal of biomedical optics, 2011. **16**(12): p. 126001-1260018.

37. van de Giessen, M., J.P. Angelo, and S. Gioux, *Real-time, profile-corrected single snapshot imaging of optical properties.* Biomedical optics express, 2015. **6**(10): p. 4051-4062.

38. Ayers, F., et al. *Fabrication and characterization of silicone-based tissue phantoms with tunable optical properties in the visible and near infrared domain*. in *Biomedical Optics (BiOS) 2008*. 2008. International Society for Optics and Photonics.

39. Choi, B., et al., *Linear response range characterization and in vivo application of laser speckle imaging of blood flow dynamics.* Journal of biomedical optics, 2006. **11**(4): p. 041129-041129-7.

40. Eliakim, M., D. Sapoznikov, and J. Weinman, *Pulse wave velocity in healthy subjects and in patients with various disease states.* American heart journal, 1971. **82**(4): p. 448-457.

41. Imholz, B.P., et al., *Fifteen years experience with finger arterial pressure monitoring.* Cardiovascular research, 1998. **38**(3): p. 605-616.

42. Allen, J. and A. Murray, *Age-related changes in the characteristics of the photoplethysmographic pulse shape at various body sites.* Physiological measurement, 2003. **24**(2): p. 297.

43. Baker, W.B., et al., *Modified Beer-Lambert law for blood flow.* Biomedical optics express, 2014. **5**(11): p. 4053-4075.

44. Briers, J.D., *Laser Doppler, speckle and related techniques for blood perfusion mapping and imaging.* Physiological measurement, 2001. **22**(4): p. R35.

45. Jacques, S.L., *Optical properties of biological tissues: a review.* Physics in medicine and biology, 2013. **58**(11): p. R37.

46. Costanzo, L.S., *Physiology*. Third ed. 2006, Philadelphia, PA: Saunders. 490.

47. Allen, J., *Photoplethysmography and its application in clinical physiological measurement.* Physiological measurement, 2007. **28**(3): p. R1.

48. DOSHI, S.N., et al., *Flow-mediated dilatation following wrist and upper arm occlusion in humans: the contribution of nitric oxide.* Clinical science, 2001. **101**(6): p. 629-635.

49. Thijssen, D.H., et al., *Reproducibility of blood flow and post-occlusive reactive hyperaemia as measured by venous occlusion plethysmography.* Clinical science, 2005. **108**(2): p. 151-157.

50. Verma, S., M.R. Buchanan, and T.J. Anderson, *Endothelial function testing as a biomarker of vascular disease.* Circulation, 2003. **108**(17): p. 2054-2059.

51. Menkes, M., et al., *Cardiovascular reactivity to the cold pressor test as a predictor of hypertension.* Hypertension, 1989. **14**(5): p. 524-530.

52. Warburton, D.E., et al., *Reliability and validity of measures of cardiac output during incremental to maximal aerobic exercise.* Sports medicine, 1999. **27**(4): p. 241-260.

53. Murray, W.B. and P.A. Foster, *The peripheral pulse wave: information overlooked.* Journal of clinical monitoring, 1996. **12**(5): p. 365-377.

54. Mardirossian, G. and R.E. Schneider, *Limitations of pulse oximetry.* Anesthesia progress, 1992. **39**(6): p. 194.

55. Hayes, M.J. and P.R. Smith, *A new method for pulse oximetry possessing inherent insensitivity to artifact.* IEEE Transactions on Biomedical Engineering, 2001. **48**(4): p. 452-461.

56. Chung, E., et al., *Non-invasive continuous blood pressure monitoring: a review of current applications.* Frontiers of medicine, 2013. **7**(1): p. 91-101.

57. Ghijsen, M., et al., *Real-time simultaneous single snapshot of optical properties and blood flow using coherent spatial frequency domain imaging (cSFDI).* Biomedical optics express, 2016. **7**(3): p. 870-882.

58. Flock, S.T., et al., *Optical properties of Intralipid: a phantom medium for light propagation studies.* Lasers in surgery and medicine, 1992. **12**(5): p. 510-519.

59. Serianni, R., et al., *Porcine-specific hemoglobin saturation measurements.* Journal of Applied Physiology, 2003. **94**(2): p. 561-566.

60. Lee, J., et al., *Non-invasive in vivo diffuse optical spectroscopy monitoring of cyanide poisoning in a rabbit model.* Physiological measurement, 2007. **28**(9): p. 1057.

61. Lee, J., et al., *Noninvasive in vivo monitoring of methemoglobin formation and reduction with broadband diffuse optical spectroscopy.* Journal of Applied Physiology, 2006. **100**(2): p. 615-622.

62. Kernick, D., J. Tooke, and A. Shore, *The biological zero signal in laser Doppler fluximetry–origins and practical implications.* Pflügers Archiv European Journal of Physiology, 1999. **437**(4): p. 624-631.

63. Nguyen, J.Q., et al., *Spatial frequency domain imaging of burn wounds in a preclinical model of graded burn severity.* Journal of biomedical optics, 2013. **18**(6): p. 066010-066010.

64. Evans, N. and P. Naylor, *The dynamics of changes in dermal oxygen tension.* Respiration physiology, 1966. **2**(1): p. 61-72.

65. Spence, V. and W. Walker, *Measurement of oxygen tension in human skin.* Medical and Biological Engineering and Computing, 1976. **14**(2): p. 159-165.